Novel OTFS System Designs for 6G Communication Networks

by

Yusuf İslam Tek

A Dissertation Submitted to the
Graduate School of Sciences and Engineering
in Partial Fulfillment of the Requirements for
the Degree of

Master of Science

in

Electrical and Electronics Engineering

KOÇ ÜNİVERSİTESİ

September 19, 2023

Novel OTFS System Designs for 6G Communication Networks

Koç University

Graduate School of Sciences and Engineering

This is to certify that I have examined this copy of a master's thesis by

Yusuf İslam Tek

and have found that it is complete and satisfactory in all respects,

and that any and all revisions required by the final

examining committee have been made.

Committee Members:

Assoc. Prof. Ertuğrul Başar (Advisor)

Prof. Alper Erdoğan

Assist. Prof. Ahmet Yazar

Date:

To my dear family,

ABSTRACT

Novel OTFS System Designs for 6G Communication Networks
Yusuf İslam Tek
Master of Science in Electrical and Electronics Engineering
September 19, 2023

Conventional modulation methods, though effective in many scenarios, encounter difficulties when dealing with high-speed communication in dynamic environments. The rapid movement of devices, along with the impacts of multipath propagation and Doppler spread, can introduce complexities that degrade communication quality. To address these challenges, the orthogonal time frequency space (OTFS) waveform emerges as an innovative solution, bridging the gap between the demands of next-generation communication technologies and the intricacies of high-speed data exchange.

OTFS represents a groundbreaking modulation technique that reimagines the approach to communication within the time-frequency domain. Unlike traditional methods, OTFS adopts a more comprehensive approach by simultaneously considering both time and frequency domains. However, there is still a need for the design of more sophisticated OTFS-based modulation schemes to meet the rigid requirements of the 6G standard. In this thesis, three performance improvement methods for OTFS are presented.

In Chapter 3, a deep learning (DL)-based technique named autoencoder (AE)-based enhanced OTFS (AEE-OTFS) to improve the error performance of OTFS is proposed. An AE structure is exploited to learn a set of high-dimensional symbols and maximize the squared minimum Euclidean distance (SMED) between them. Unlike complex doubly-dispersive channels, this AE is trained under the simpler conditions of an additive white Gaussian noise (AWGN) channel. The encoder and decoder of AE are then repurposed as the mapper and demapper blocks in a real-time OTFS system. The approach also establishes a theoretical frame error rate (FER) upper bound. Simulation results demonstrate that AEE-OTFS outperforms conventional OTFS in terms of FER performance. The addition of a learned detector (LD) significantly reduces decoding complexity. These findings suggest that AEE-

OTFS holds promise for certain 6G applications, particularly in high-mobility and flexible scenarios.

In Chapter 4, a block-wise index modulation (IM) technique named joint delay-Doppler IM-based OTFS (JDDIM-OTFS) is designed to enhance the error performance of OTFS. In this chapter, a theoretical upper bound on the bit error rate (BER) is also established. Computer simulations reveal that JDDIM-OTFS surpasses conventional OTFS, OTFS-IM, and delay-IM OTFS (DeIM-OTFS) systems in terms of BER when combined with matched-filtered Gauss-Seidel (MFGS) detector with a maximum likelihood detector (MFGS-ML) and MFGS with a greedy detector (MFGS-GRD). The adoption of a Greedy detector within MFGS substantially reduces decoding complexity. JDDIM-OTFS exhibits remarkable error performance in scenarios characterized by high mobility and flexibility, making it an exciting choice for specific 6G use cases.

Finally, in Chapter 5, for reducing the peak-to-average power ratio (PAPR) of OTFS, a method is suggested that utilizing unitary transformations such as Walsh-Hadamard transform (WHT), Zadoff-Chu transform (ZCT), and discrete cosine transform (DCT). The performance of this method is evaluated across various frame sizes and compared to clipping and discrete Fourier transform-spread (DFT-s OTFS) techniques. Additionally, the impact of this approach on BER performance is assessed against other methods. Computer simulations demonstrate that this proposed method significantly reduces PAPR while introducing a compromise of approximately 1.5 dB in error performance. The substantial PAPR reduction, coupled with the absence of the need for receiver-side information, highlights the significance of this approach.

ÖZETÇE

6G Haberleşme Ağları için Yeni OTFS Sistem Tasarımları
Yusuf İslam Tek
Elektrik ve Elektronik Mühendisliği, Yüksek Lisans
19 Eylül 2023

Geleneksel modülasyon yöntemleri, birçok senaryoda etkili olsa da, yüksek hızlı iletişimde dinamik ortamlarla başa çıkmakta zorluklarla karşılaşır. Alıcı ya da verici ekipmanların hızlı hareketi, çoklu yol yayılması ve Doppler yayılmasının etkileri, iletişim kalitesini düşüren etkenlerden bazılarıdır. Bu problemlere cevap olarak, dikgen zaman frekans uzayı (orthogonal time frequency space, OTFS) dalga şekli, gelecek nesil iletişim teknolojilerinin gereksinimleri ile yüksek hızlı veri alışverişinin karmaşıklıklarının üstesinden gelebilen yenilikçi bir çözüm olarak ortaya çıkmıştır.

OTFS, zaman frekans alanında iletişime yaklaşımı yeniden tasarlayan devrim niteliğinde bir modülasyon tekniğidir. Geleneksel yöntemlerin aksine, OTFS, hem zaman hem de frekans alanlarını aynı anda kullanarak Doppler yayılmasına karşı üstün performans gösterir. Ancak, 6G standardının katı gereksinimlerini karşılamak için daha sofistike OTFS tabanlı modülasyon şemalarının tasarımına olan ihtiyaç hala devam etmektedir. Bu tezde, OTFS için üç performans iyileştirme yöntemi sunulmaktadır.

3. Bölümde, OTFS'in hata performansını iyileştirmek için derin öğrenmeye (deep learning, DL) dayalı otomatik kodlayıcı (autoencoder, AE) tabanlı iyileştirişmiş OTFS (AEE-OTFS) isimli yeni bir teknik önerilmektedir. Bir AE yapısı, yüksek boyutlu sembollerin öğrenilmesi ve aralarındaki en küçük Öklid mesafesini maksimize etmek için kullanılmıştır. Karmaşık zamanla değişen kanalların aksine, bu AE yapısı, toplanır beyaz Gauss gürültüsü (additive white Gaussian noise, AWGN) kanalının daha basit koşulları altında eğitilmektedir. AE'ın kodlayıcısı ve kod çözücüsü daha sonra gerçek zamanlı bir OTFS sisteminde sembol eşleme ve sembol çözme blokları olarak yeniden kullanılır. Çalışmada aynı zamanda teorik bir paket hata oranı (frame error rate, FER) üst sınırı türetilmiştir. Simülasyon sonuçları, AEE-OTFS'in FER performansı açısından geleneksel OTFS'i geçtiğini göstermektedir. Öğrenilen bir dedektörün (learned detector, LD) eklenmesi, kod çözme karmaşıklığını

önemli ölçüde azaltır. Bu bulgular, AEE-OTFS'nin özellikle yüksek hareketlilik ve esneklik senaryolarında belirli 6G uygulamaları için umut vadettiğini göstermektedir.

4. Bölümde, OTFS'nin hata performansını artırmak için ortak gecikme-Doppler indeks modülasyonu tabanlı OTFS (JDDIM-OTFS) tekniği tasarlanmıştır. Bu bölümde aynı zamanda bit hata oranı (BER) üzerine teorik bir üst sınır da belirlenmiştir. Bilgisayar simülasyonları, JDDIM-OTFS'nin, eşleştirilmiş filtreli Gauss-Seidel (matched-filtered Gauss-Seidel, MFGS) dedektörü ile maksimum olabilirlik dedektörü (MFGS-ML) ve MFGS ile aç gözlü bir dedektör (MFGS-GRD) ile birleştirildiğinde BER açısından geleneksel OTFS, OTFS-IM ve gecikme-IM OTFS (delay-IM, DeIM-OTFS) sistemlerini geride bıraktığını göstermektedir. MFGS içinde Aç Gözlü bir dedektörün kullanılması kod çözme karmaşıklığını önemli ölçüde azaltır. JDDIM-OTFS, yüksek hareketlilik ve esneklikle karakterize edilen senaryolarda dikkate değer bir hata performansı sergileyerek, belirli 6G kullanım durumları için heyecan verici bir seçenek haline gelmektedir.

Son olarak, 5. bölümde, OTFS'in tepe-ortalama güç oranını (peak-to-average power ratio, PAPR) azaltmak için Walsh-Hadamard dönüşümü (Walsh-Hadamard transform, WHT), Zadoff-Chu dönüşümü (Zadoff-Chu transform, ZCT) ve ayrık kosinüs dönüşümü (discrete cosine transform, DCT) gibi ünitersel dönüşümleri kullanma önerilmektedir. Bu yöntemin farklı çerçeve boyutları üzerindeki performansı ve kırpma ve ayrık Fourier dönüşümü-s (discree Fourier transform-spread OTFS, DFT-s OTFS) teknikleri ile karşılaştırılması yapılmaktadır. Ayrıca, bu yaklaşımın BER performansına diğer yöntemlere göre etkisi değerlendirilir. Bilgisayar simülasyonları, bu önerilen yöntemin PAPR'ı önemli ölçüde azalttığını gösterirken, hata performansında yaklaşık olarak 1.5 dB'lik bir kayıp yaşandığını göstermektedir. Yüksek PAPR azaltmanın yanı sıra, alıcı tarafındaki bilgiye ihtiyaç duyulmaması bu yaklaşımı önemli bir yaklaşım haline getirir.

ACKNOWLEDGMENTS

First of all, I want to extend my sincere gratitude to my dear advisor, Dr. Ertuğrul Başar, for their invaluable guidance and support throughout my master's degree journey. His expertise, encouragement, and mentorship have been instrumental in shaping my academic and personal growth. I am truly fortunate to have had such a dedicated and inspiring advisor.

Secondly, I would like to express my deepest appreciation and gratitude to my lovely mother Afet, my dear father Ziyaettin, and my dear sisters and brothers for their unwavering love, support, and encouragement. I love you all deeply, and this achievement is as much yours as it is mine.

Finally, I would also thank all of my wonderful friends in CoreLab. Your friendship has been an incredible journey filled with laughter, support, and countless cherished memories. Thank you for being such amazing friends.

TABLE OF CONTENTS

LIST OF TABLES

LIST OF FIGURES

ABBREVIATIONS

6G	Sixth-Generation
AE	Autoencoder
AWGN	Additive White Gaussian Noise
BER	Bit Error Rate
CCDF	Complementary Cumulative Distribution Function
CPEP	Conditional Pairwise Error Probability
CSI	Channel State Information
DCT	Discrete Cosine Transform
DL	Deep Learning
DNN	Deep Neural Network
EVA	Extended Vehicular A
FER	Frame Error Rate
IEEE	The Institute of Electrical and Electronics Engineers
IM	Index Modulation
IoT	Internet of Things
ISFFT	Inverse Symplectic Finite Fourier Transform
ISI	Inter-Symbol Interference
LD	Learned Detector
MFGS	Matched-Filtered Gauss-Seidel
ML	Maximum Likelihood
MMSE	Minimum Mean Squared Error
NN	Neural Network
OFDM	Orthogonal Frequency Division Multiplexing
OTFS	Orthogonal Time Frequency Space
PAPR	Peak-to-Average Power Ratio

PEP	Pairwise Error Probability
PSK	Phase Shift Keying
QAM	Quadrature Amplitude Modulation
SE	Spectral Efficiency
SFFT	Symplectic Finite Fourier Transform
SMED	Squared Minimum Euclidean Distance
SNR	Signal-to-Noise Ratio
UPEP	Unconditional Pairwise Error Probability
WHT	Walsh-Hadamard Transform
ZCT	Zadoff-Chu Transform
ZP	Zero-Padding

Chapter 1

INTRODUCTION

In the dynamic landscape of modern communication technologies, the advent of next-generation communication systems is ushering in a transformative era of connectivity. These systems are engineered to meet the surging demand for high-speed, low-latency communication, addressing the ever-expanding array of applications that rely on seamless and reliable data exchange. The surge in data-driven applications, driven by the proliferation of Internet-connected devices, streaming services, and the Internet-of-Things (IoT), has necessitated communication technologies capable of delivering data at unprecedented speeds. This surge, along with the proliferation of emerging technologies like autonomous vehicles, augmented reality, and telemedicine, which are also being considered for sixth-generation (6G) use cases, has fueled the demand for communication systems that can provide not only fast data transfer but also low latency and robust connectivity.

Traditional modulation schemes, while well-suited to many scenarios, face challenges when confronted with high-speed communication in dynamic environments. The high mobility of devices, coupled with the effects of multipath propagation and Doppler spread, can introduce complexities that degrade the quality of communication links. In response to these challenges, the orthogonal time frequency space (OTFS) waveform [Hadani et al., 2017] emerges as a groundbreaking solution, bridging the gap between the demands of next-generation communication technologies and the intricacies of high-speed data exchange.

OTFS is a revolutionary modulation technique that reimagines the way to approach communication in the time-frequency domain. Unlike traditional schemes that rely solely on variations in amplitude, phase, or frequency, OTFS takes a more holistic approach by simultaneously considering both time and frequency domains. By doing so, it introduces a unique spatial-temporal framework that enables communication systems to thrive in the face of dynamic channel conditions.

In this thesis, by utilizing deep learning (DL), index modulation (IM), and the unitary matrices, three novel solutions are presented in order to improve the performance metrics of OTFS modulation.

1.1 Contributions

In the thesis, firstly, we propose an autoencoder (AE)-based scheme called *AE-based enhanced OTFS (AEE-OTFS)* that models the mapper and learned demapper of an OTFS system as the encoder and decoder of an AE, respectively. Here, the AE is trained offline in an additive white Gaussian noise (AWGN) channel so that the encoder of AE provides a set of n-dimensional (n-dim) symbols that maximize squared minimum Euclidean distance (SMED) between them. Furthermore, the decoder of AE enables low-complexity detection of n-dim symbols of the equalized OTFS signal on the receiver side. Note that the modulator and demodulator blocks can be learned using the OTFS framework under a doubly-dispersive channel rather than an AWGN channel; however, this causes the AE structure to be more complex and increases training time. We train our AE-based scheme over the AWGN channel, which does not include the doubly-dispersive channel and signal-processing blocks of the OTFS transceiver in the training process. Additionally, we derive a theoretical upper bound for the frame error rate (FER).

Secondly, we propose a scheme called *joint delay-Doppler index modulation (IM)-based OTFS (JDDIM-OTFS)* to combat doubly-dispersive channel effects and further improve the error performance. Here, we use a zero-padded (ZP) OTFS system to eliminate inter-block interference and have better error performance. We design a block-wise IM scheme that activates delay or Doppler resource blocks. To further improve the spectral efficiency (SE), we suggest using different constellations on different active resource blocks. Moreover, we use a matched-filtered Gauss-Seidel (MFGS) detector with a maximum likelihood detector (MFGS-ML) and a low-complex greedy detector (MFGS-GRD) to decode information bits. Also, we derive a theoretical upper bound for JDDIM-OTFS to verify our results.

Finally, we suggest using unitary precoding matrices to reduce the peak-to-average power ratio (PAPR) of OTFS modulation and investigate the effect of these matrices. We apply the Zadoff-Chu transform (ZCT), Walsh-Hadamard transform (WHT), and discrete cosine transform (DCT) to the time domain OTFS signal to reduce the PAPR by exploiting the peak reduction properties of these transforms. Computer simulation results show that, even though we obtain remarkable PAPR performance gain, there is a slight bit error rate (BER) deterioration due to residual interference from the time-varying channel.

The two of these contributions have been published in the Institute of Electrical and Electronics Engineers (IEEE) journals and in an IEEE conference. AEE-OTFS has been published in *IEEE Communications Letters*. PAPR reduction precoding work has been presented at *IEEE 2023 46th International Conference on Telecommunications and Signal Processing (TSP 2023)*. JDDIM-OTFS has been submitted to IEEE.

Notations: a, $\mathbf{a}$, and $\mathbf{A}$ stand for a scalar, a vector, and a matrix, respectively. $\mathbf{a}(i)$ and $\mathbf{A}(i, j)$ represent i-th element of $\mathbf{a}$ and (i, j)-th elemenf of $\mathbf{A}$, respectively. $\mathbf{I}_N$ is the $N \times N$ identity matrix. $\mathbf{A} = \mathrm{diag}([a_0, \dots, a_M])$ denotes a diagonal matrix with diagonal elements $[a_0, \dots, a_M]$. $\mathrm{C}(n, k)$ is the binomial coefficient that chooses k out of n. $\delta(\cdot)$ and $Q(\cdot)$ refer to the Dirac delta function and the Gaussian tail function, respectively. The superscripts $(\cdot)^{\mathrm{T}}$ and $(\cdot)^{\mathrm{H}}$ state the transpose and the Hermitian transpose operators, respectively. The operators $\otimes$, $\|\cdot\|$, $|\cdot|$, $E\{\cdot\}$ and $\Re\{\cdot\}$ represent the Kronecker product, Euclidean norm, the cardinality of a set, the expectation, and the real part operators, respectively. $\langle\cdot\rangle$ is the sample mean operator for vectors. The determinant and the rank of a matrix are denoted by $\det(\cdot)$ and $\mathrm{rank}(\cdot)$, respectively. The zero mean circular symmetric complex Gaussian distribution with variance σ^2 is denoted by $\mathcal{CN}(0, \sigma^2)$. Finally, $\mathbf{F}_N$ refers to the N point normalized DFT matrix.

Chapter 2

ORTHOGONAL TIME FREQUENCY SPACE MODULATION

OTFS modulation is an innovative modulation scheme that has garnered significant attention in the field of wireless communications. Unlike traditional modulation techniques, OTFS operates in a domain where both time and frequency are simultaneously manipulated to combat the challenges posed by time-varying channels [Hadani et al., 2017]. This modulation scheme exhibits remarkable resilience in high-mobility environments, making it a promising candidate for next-generation wireless communication systems. In this chapter, we will describe the system model of OTFS modulation, and we will present a brief literature review of OTFS modulation.

2.1 OTFS System Model

We consider an OTFS transmission system with a bandwidth of $M\Delta f$ and a total frame duration of NT, where $M, N, \Delta f$, and T are the number of subcarriers, number of symbols, subcarrier spacing, and symbol duration, respectively. The transceiver diagram is given in Fig. 2.1. First, the information bits are mapped to MN delay-Doppler domain Q-ary symbols. Then, these symbols are placed into delay-Doppler domain information symbol matrix $\mathbf{X} \in \mathbb{C}^{M\times N}$. The delay-Doppler domain information symbols are converted into time-frequency domain symbols by performing inverse symplectic finite Fourier transform (ISFFT) as

$$\bar{\mathbf{X}}(n,m) = \frac{1}{\sqrt{MN}} \sum_{k=0}^{N-1} \sum_{l=0}^{M-1} \mathbf{X}(k,l) e^{j2\pi\left(\frac{nk}{N} - \frac{ml}{M}\right)}. \tag{2.1}$$

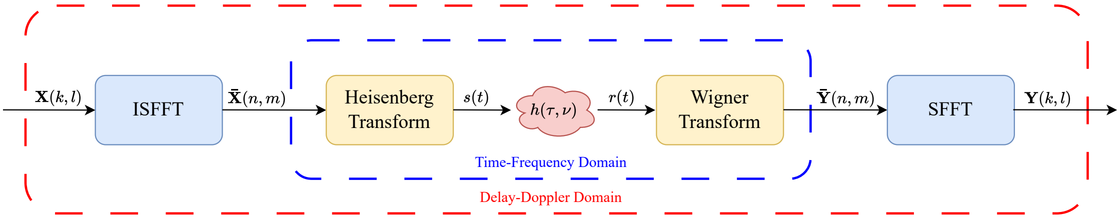

Figure 2.1: Transceiver scheme of an OTFS system.

Next, time-frequency domain symbols are transformed into time-domain signal $s(t)$ by utilizing the Heisenberg transform and applying 2-D windowing as

$$s(t) = \sum_{n=0}^{N-1} \sum_{m=0}^{M-1} \bar{\mathbf{X}}(n,m) g_{\mathrm{tx}}(t-nT) e^{j2\pi m \Delta f (t-nT)}. \tag{2.2}$$

Later, $s(t)$ is transmitted over a doubly-dispersive channel. The channel impulse response of the doubly-dispersive channel is given by

$$h(\tau,\nu) = h(\tau,\nu) = \sum_{i=1}^{P} h_i \delta(\tau-\tau_i)\delta(\nu-\nu_i), \tag{2.3}$$

where P is the number of propagation paths, h_i, τ_i and ν_i stand for the complex channel gain, delay shift, and Doppler shift for the ith path, respectively.

At the receiver side, Wigner transform is employed to the received signal $r(t)$ as

$$\bar{\mathbf{Y}}(n,m) = \left[\int g_{\mathrm{rx}}^{*}(t-\tau) r(t) e^{j2\pi\nu(t-\tau)} dt \right] |_{\tau=nT, \nu=m\Delta f}. \tag{2.4}$$

Then, in order to obtain delay-Doppler domain information symbols, the SFFT transform is performed to $\bar{\mathbf{Y}}$ as

$$\mathbf{Y}(k,l) = \frac{1}{\sqrt{MN}} \sum_{n=0}^{N-1} \sum_{m=0}^{M-1} \bar{\mathbf{Y}}(n,m) e^{-j2\pi\left(\frac{nk}{N} - \frac{ml}{M}\right)}. \tag{2.5}$$

2.2 A Brief Literature Survey on OTFS

OTFS has attracted significant interest from researchers due to its robustness against the time-varying channels. The researchers in [Surabhi et al., 2019a] show that the asymptotic diversity order of the OTFS for high signal-to-noise (SNR) values is one. Then, in [Raviteja et al., 2020], the authors derive an upper bound on the average BER and prove that the OTFS can achieve full effective diversity P in the intermediate SNR region when the OTFS frame is sufficiently large. The performance of OTFS on the static multipath channels is investigated in [Raviteja et al., 2019]. In static multipath channel environments, the system architecture of OTFS is analogous to asymmetric orthogonal frequency division multiplexing (A-OFDM), a scheme introduced in [Zhang et al., 2007]. The comprehensive derivation of OTFS with ZAK representation from first principles is presented in [Mohammed, 2021]. In [Li et al., 2021], based on conditional pairwise-error probability (PEP), a performance upper bound of the coded OTFS system is studied. The researchers show that the enhancement in coding performance for OTFS systems is influenced by both the squared Euclidean distance among codeword pairs and the number of independent resolvable paths within the channel.

In order to reach the next-generation communications systems requirements, many studies have been presented in the literature to improve the error performance or reduce the decoding complexity of the OTFS system by exploiting DL. Deep neural network (DNN) based techniques have been presented for signal detection in [Naikoti and Chockalingam, 2021, Xu et al., 2020]. Additionally, in [Liu et al., 2023], the authors introduced an intelligent DNN-based precoding method that can maintain high reliability without the need for instantaneous Channel State Information (CSI). The researchers in [Zhou et al., 2022] propose a neural network-based supervised learning framework utilizing reservoir computing for OTFS equalization. This introduced method for OTFS is expected to result in an improved trade-off between processing complexity and equalization performance. A performance improvement scheme based on AE is presented in [Park et al., 2023]. The authors utilize the AE architecture by dividing the OTFS frame into subframes since the whole OTFS frame is hard to use in AE.

IM is among the popular modulation techniques due to the energy and SE it provides. Classic IM is first proposed in [Liang et al., 2020] for OTFS. In this work, the index bits are conveyed by activating or deactivating the delay-Doppler domain resource elements. Dual-mode and multiple-mode OTFS-IM schemes with a low-complex detector have been proposed in [Zhao et al., 2021] and [Ren et al., 2022], respectively. Furthermore, in [Feng et al., 2022], the authors proposed a scheme in which additional information bits are carried through the grid index of the OTFS block in in-phase and quadrature dimensions. Besides, a scheme that transmits selected indices with double subblocks and different symbols is proposed in [Ren et al., 2021]. Moreover, in [Qian et al., 2023], the authors introduced an innovative block-wise IM scheme for OTFS, where a set of delay/Doppler resource bins are activated simultaneously. In order to decode information bits in those blocks more efficiently, the authors have also proposed two message-passing algorithm-based low-complex detectors. Also, a diversity enhancing and PAPR reduction scheme that uses IM is proposed in [Francis et al., 2021].

PAPR reduction techniques have been extensively studied for other modulation schemes, such as OFDM, and many of these techniques have been successfully applied in practical systems [Han and Lee, 2005]. However, for OTFS, the literature is not rich on PAPR reduction techniques. The PAPR analysis of OTFS has been studied in [Surabhi et al., 2019b], and in [Wei et al., 2022], the parameters that affect the PAPR have been examined. In [Gao and Zheng, 2020], a pilot-supported iterative clipping-based PAPR reduction method has been proposed. The aim is to take advantage of the available space in the guard area by incorporating dither signals, which can help decrease the PAPR. Also, in [Bitra et al., 2022a, Naveen and Sudha, 2020, Bitra et al., 2022b], μ-law, A-law, and nonlinear companding-based PAPR reduction techniques have been proposed. While clipping and companding techniques improve the PAPR performance, they can lead to a degradation in the BER performance due to signal distortion [Tek et al., 2020]. Moreover, in [Wu et al., 2021] and [Hossain et al., 2020], the performance is improved by employing the delay-Doppler domain discrete Fourier transform-spread (DFT-s) precoding method. Furthermore, in [Su et al., 2022], a symbol-precoding-based PAPR reduction scheme has been proposed. The objective is to create an ideal precoding matrix that reduces the fluctuation in instantaneous power while ensuring that reliable communication data transmission is not compromised. The authors in [Sümer et al., 2022], propose a peak-reducing technique by exploiting the properties of the

OTFS frame. In this method, the time domain OTFS signal is divided into subblocks, and complex constants are added to the subblocks to reduce peak values. The authors in [Liu et al., 2021] introduce a method for PAPR reduction utilizing a deep neural network technique known as autoencoder. The trained encoder and decoder components of the autoencoder serve to lower the PAPR and reconstruct the signal, respectively.

Chapter 3

AUTOENCODER-BASED ENHANCED ORTHOGONAL TIME FREQUENCY SPACE MODULATION

It is well known that OTFS provides superior performance in doubly-dispersive channels. Since it spreads information symbols across the entire delay-Doppler plane, OTFS can achieve full diversity. However, reliability still needs to be improved in OTFS systems to meet the stringent demands of future communication systems. To address this issue, we propose an AEE-OTFS modulation scheme. By training an AE under an AWGN channel, a feasible mapper and demapper are learned to improve the error performance and decrease the detection complexity of the OTFS system. The learned mapper is used to map incoming bits into high-dimensional symbols while the learned demapper recovers the information bits in the delay-Doppler domain.

In this chapter, the system model, performance analysis, and simulation results of AEE-OTFS are given.

3.1 System Model of AEE-OTFS

In this section, first, we describe the transceiver scheme of the proposed AEE-OTFS system, and then, we explain the details of the proposed AE-based neural network (NN).

3.1.1 Transmission of AEE-OTFS

We consider an AEE-OTFS transmission system with N symbols and M subcarriers, where its block diagram is given in Fig. 3.1. In this OTFS-based scheme, Δf and $T = 1/\Delta f$ represent subcarrier spacing and symbol duration, respectively. A total number of b bits enter the system. These bits are then split into G groups,

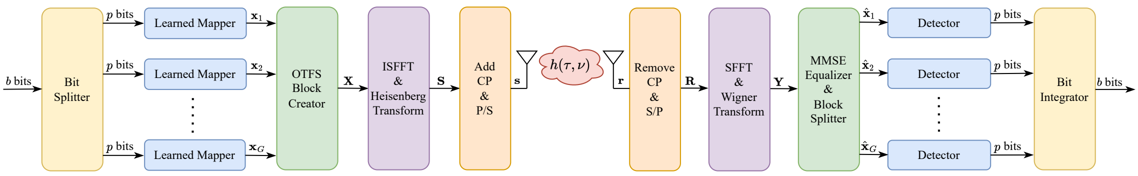

Figure 3.1: Transceiver scheme of AEE-OTFS system.

each including $p = b/G = \log_2(|\mathcal{X}|)$ bits, where $\mathcal{X}$ is the set of all possible n-dim symbols. For the gth group, p bits are mapped into an n-dim symbol, $\mathbf{x}_g \in \mathbb{C}^{n\times 1}$, $g = 1, 2, \cdots, G$, where $\mathbf{x}_g \in \mathcal{X}$. The steps of this mapper are discussed in the sequel. All selected n-dim symbols are concatenated as $\mathbf{x} = [\mathbf{x}_1^{\mathrm{T}}, \mathbf{x}_2^{\mathrm{T}}, \cdots, \mathbf{x}_G^{\mathrm{T}}]^{\mathrm{T}}$ and $\mathbf{x}$ is provided to the OTFS block creator and overall delay-Doppler domain OTFS frame is obtained as $\mathbf{X} \in \mathbb{C}^{M\times N}$. In the next step, $\mathbf{X}$ is converted to the time-frequency domain by using ISFFT, and after, using the Heisenberg transform with pulse-shaping waveform $g_{\mathrm{tx}}(t)$, time-domain transmit signal is obtained as

$$\mathbf{S} = \mathbf{G}_{\mathrm{tx}}\mathbf{F}_M^{\mathrm{H}}(\mathbf{F}_M\mathbf{X}\mathbf{F}_N^{\mathrm{H}}) = \mathbf{G}_{\mathrm{tx}}\mathbf{X}\mathbf{F}_N^{\mathrm{H}}, \tag{3.1}$$

where $\mathbf{G}_{\mathrm{tx}} = \mathrm{diag}[g_{\mathrm{tx}}(0), g_{\mathrm{tx}}(T/M), \ldots, g_{\mathrm{tx}}((M-1)T/M)] \in \mathbb{C}^{M\times M}$. For transmission, a column-wise vectorization is applied to $\mathbf{S} \in \mathbb{C}^{M\times N}$, and the transmit vector $\mathbf{s} \in \mathbb{C}^{MN\times 1}$ is transmitted over the time-varying channel. Before transmission, a CP is added to $\mathbf{s}$ in order to prevent inter-symbol interference (ISI). The time-varying channel with response is represented by $h(\tau,\nu) = \sum_{i=1}^{P} h_i\delta(\tau-\tau_i)\delta(\nu-\nu_i)$, where P is the number of propagation paths, h_i, τ_i and ν_i stand for the complex channel gain, delay shift, and Doppler shift for the ith path, respectively. At the receiver, after discarding CP, the received time domain signal can be expressed as $\mathbf{r} = \mathbf{H}\mathbf{s} + \mathbf{w}$, where $\mathbf{w} \in \mathbb{C}^{MN\times 1}$ is a vector of zero mean AWGN samples with $\mathcal{CN}(0, N_0\mathbf{I}_{MN})$, N_0 is the noise variance, and $\mathbf{H} \in \mathbb{C}^{MN\times MN}$ is the time domain channel matrix given by

$$\mathbf{H} = \sum_{i=1}^{P} h_i \mathbf{\Pi}^{l_i}\mathbf{\Delta}^{k_i+\kappa_i}, \tag{3.2}$$

where $\mathbf{\Pi} = \mathrm{circ}\{[0, 1, \ldots, 0]^{\mathrm{T}}\} \in \mathbb{R}^{MN\times MN}$ is the cyclic-shift matrix and $\mathbf{\Delta} = \mathrm{diag}[1, e^{-2\pi j/MN}, \ldots, e^{-2\pi j(MN-1)/MN}] \in \mathbb{C}^{MN\times MN}$ represents the diagonal Doppler

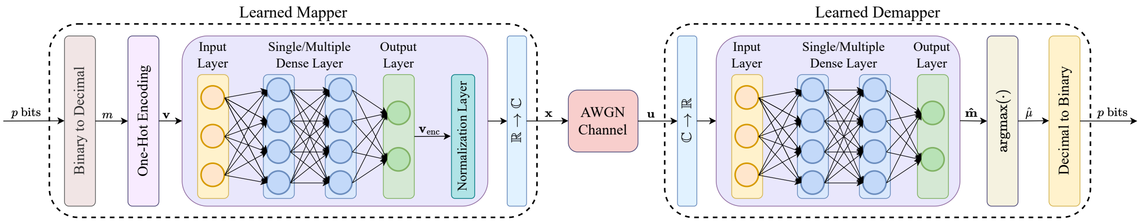

Figure 3.2: The structure of the proposed AE.

shift matrix. We define the fading parameters for the ith path as $h_i \sim \mathcal{CN}(0, 1/P)$, $\tau_i = \frac{l_i}{M\Delta f}$, $\nu_i = \frac{k_i+\kappa_i}{NT}$ where l_i, k_i and κ_i represent delay taps, Doppler taps, and fractional Doppler shift, respectively. We assume that l_i and k_i are integers and there is no fractional Doppler shift, $\kappa_i = 0$.

After the signal is received, $\mathbf{r}$ is de-vectorized and converted to a matrix $\mathbf{R}$ with the size of $M \times N$. Then, the delay-Doppler domain received signal $\mathbf{Y}$ is obtained by applying Wigner transform and SFFT to $\mathbf{R}$ and it can be expressed as:

$$\mathbf{Y} = \mathbf{F}_M^{\mathrm{H}}(\mathbf{F}_M \mathbf{G}_{\mathrm{rx}} \mathbf{R})\mathbf{F}_N = \mathbf{G}_{\mathrm{rx}} \mathbf{R} \mathbf{F}_N. \tag{3.3}$$

Moreover, by combining (3.1) and (3.3), the vectorization of $\mathbf{Y}$ can be given as:

$$\mathbf{y} = (\mathbf{F}_N \otimes \mathbf{G}_{\mathrm{rx}})\mathbf{H}(\mathbf{F}_N^{\mathrm{H}} \otimes \mathbf{G}_{\mathrm{tx}})\mathbf{x} + \tilde{\mathbf{w}} = \mathbf{H}_{\mathrm{eff}}\mathbf{x} + \tilde{\mathbf{w}}, \tag{3.4}$$

where $\mathbf{H}_{\mathrm{eff}} \in \mathbb{C}^{MN \times MN}$ is the effective delay-Doppler domain channel matrix and $\tilde{\mathbf{w}}$ is the noise in delay-Doppler domain. In case of rectangular waveforms (i.e., $\mathbf{G}_{\mathrm{rx}} = \mathbf{I}_M$), $\tilde{\mathbf{w}}$ has the same statistical properties of $\mathbf{w}$. By exploiting the minimum mean square error (MMSE) equalizer, the delay-Doppler domain data symbols equalized are obtained as

$$\hat{\mathbf{x}} = \mathbf{H}_{\mathrm{eff}}^{\mathrm{H}}(\mathbf{H}_{\mathrm{eff}}\mathbf{H}_{\mathrm{eff}}^{\mathrm{H}} + N_0 \mathbf{I}_{MN})^{-1}\mathbf{y} = [\hat{\mathbf{x}}_1^{\mathrm{T}}, \cdots, \hat{\mathbf{x}}_G^{\mathrm{T}}]^{\mathrm{T}}. \tag{3.5}$$

Finally, the gth equalized group $(\hat{\mathbf{x}}_g^{\mathrm{T}})$ is input to the LD or maximum-likelihood (ML) detector to decode the information bits. The above process is performed for each group.

3.1.2 AE-Based Mapper and Demapper

In this section, we present the proposed mapper and demapper for OTFS systems. In the AEE-OTFS method, we exploit the AE technique to model the mapper and demapper as two different DNNs. Here, the LM and LD are considered the encoder and decoder of an AE-based system, respectively. Since the OTFS system already provides a full diversity [Raviteja et al., 2020], to enhance the error performance of any OTFS system, one can increase the SMED, which is given by $d^2_{\min} = \min_{\mathbf{x}_\phi \neq \mathbf{x}_\varphi} \|\mathbf{x}_\phi - \mathbf{x}_\varphi\|^2$, where $\mathbf{x}_\zeta$ is the ζth n-dim symbol, $\zeta = 1, \cdots, |\mathcal{X}|$. Here, our proposed AE-based system is trained under an AWGN channel and learns a set of n-dim symbols ($\mathcal{X}$) that maximizes the SMED.

As seen from Fig. 3.2, firstly, a total number of p bits are converted into a decimal number m, $m \in \{m_1, \cdots, m_{|\mathcal{X}|}\}$. Then, m is encoded as a one-hot vector $\mathbf{v} \in \mathbb{R}^{|\mathcal{X}|\times 1}$ whose only single element is one where the others are all zeros. Then, $\mathbf{v}$ is passed through single or multiple dense layers to obtain a transmit vector $\mathbf{v}_{\text{enc}} \in \mathbb{R}^{2n\times 1}$. This encoding process can be expressed as a function $\mathbf{v}_{\text{enc}} = f_{\Omega_{\text{enc}}}(\mathbf{v})$, where Ω_{enc} is the parameter set of dense layers of encoder NN. Then, we utilize a normalization layer to satisfy energy constraints, i.e., $\|\mathbf{v}_{\text{enc}}\|^2 = n$. Moreover, $\mathbf{v}_{\text{enc}}$ is converted into a complex vector $\mathbf{x} \in \mathbb{C}^{n\times 1}$, where the first and second halves of $\mathbf{v}_{\text{enc}}$ represent the real and imaginary parts of $\mathbf{x}$, respectively. After that, $\mathbf{x}$ is transmitted over an AWGN channel and $\mathbf{u} = \mathbf{x} + \bar{\mathbf{w}}$ is obtained, where $\bar{\mathbf{w}}$ is the vector of AWGN samples whose elements follow the distribution $\mathcal{CN}(0, \bar{N}_0)$ and $\bar{N}_0$ is the noise variance. The training signal-to-noise ratio (SNR) is $\rho = 1/\bar{N}_0$. At the demapper side, $\mathbf{u}$ is first converted into a real-valued vector with dimensions $2n \times 1$ by separating the real and imaginary parts and then concatenating them. After that, it is passed through single or multiple dense layers to obtain $\mathbf{v}_{\text{dec}} \in \mathbb{R}^{|\mathcal{X}|\times 1}$. This process can be represented as a function $\mathbf{v}_{\text{dec}} = f_{\Omega_{\text{dec}}}(\mathbf{u})$, Ω_{dec} is the parameter set of dense layers of decoder NN. The softmax function is used for the output layer of decoder NN to output a probability vector $\hat{\mathbf{m}} = [\hat{m}_1, \hat{m}_2, \cdots, \hat{m}_{|\mathcal{X}|}]^{\mathrm{T}}$, where the μth element of $\hat{\mathbf{m}}$ denotes the probability of message m_μ being transmitted. The index of the transmitted message is determined as $\hat{\mu} = \underset{\mu\in\{1,\cdots,|\mathcal{X}|\}}{\operatorname{argmax}} (\hat{m}_\mu)$, and $\hat{\mu}$ is converted into bits.

To train the AE model offline, a set of randomly generated bits and noise vectors are used. We employ the categorical cross-entropy loss function and adaptive moment estimation (Adam) optimizer. Once the training stage of AE is performed, the learned mapper and demapper can be implemented in the AEE-OTFS scheme as in Fig. 3.1. As seen in Fig. 3.2, the learned mapper takes p bits as input and outputs the n-dim symbol, whereas the learned demapper takes the complex symbol vector as input and outputs p bits.

3.2 Performance Analysis

In this section, for the AEE-OTFS, we obtain an upper bound on the FER by using ML detector.

According to (3.4), under the assumption of rectangular pulses, the received signal can be expressed as

$$\begin{aligned}\mathbf{y} &= \sum_{i=1}^{P} h_i(\mathbf{F}_N \otimes \mathbf{I}_M)\mathbf{\Pi}^{l_i}\mathbf{\Delta}^{k_i}(\mathbf{F}_N^{\mathrm{H}} \otimes \mathbf{I}_M)\mathbf{x} + \tilde{\mathbf{w}} \\ &= \mathbf{\Phi}(\mathbf{x})\mathbf{h} + \tilde{\mathbf{w}}, \end{aligned} \tag{3.6}$$

where $\mathbf{h} = [h_1, h_2, \ldots, h_P]^{\mathrm{T}} \in \mathbb{C}^{P\times 1}$ is the channel gain vector, and $\mathbf{\Phi}(\mathbf{x}) \in \mathbb{C}^{MN\times P}$ is a concatenated matrix given by $\mathbf{\Phi}(\mathbf{x}) = [\mathbf{\Psi}_1\mathbf{x}, \mathbf{\Psi}_2\mathbf{x}, \ldots, \mathbf{\Psi}_P\mathbf{x}]$ and $\mathbf{\Psi}_i \triangleq (\mathbf{F}_N \otimes \mathbf{I}_M)\mathbf{\Pi}^{l_i}\mathbf{\Delta}^{k_i}(\mathbf{F}_N^{\mathrm{H}} \otimes \mathbf{I}_M)$.

We assume that perfect CSI is available at the receiver. When $\mathbf{x}$ is transmitted and erroneously detected $\hat{\mathbf{x}}$, the corresponding conditional PEP can be expressed as

$$P(\mathbf{x} \to \hat{\mathbf{x}}|\mathbf{h}) = Q\left(\sqrt{\frac{\|(\mathbf{\Phi}(\hat{\mathbf{x}}) - \mathbf{\Phi}(\mathbf{x})\mathbf{h})\|^2}{2N_0}}\right) = Q\left(\sqrt{\frac{\mathbf{\Theta}}{2N_0}}\right), \tag{3.7}$$

where $\Theta = \mathbf{h}^{\mathrm{H}}\mathbf{\Gamma}(\bar{\mathbf{x}})\mathbf{h}$, $\mathbf{\Gamma}(\bar{\mathbf{x}}) = \mathbf{\Phi}(\bar{\mathbf{x}})^{\mathrm{H}} - \mathbf{\Phi}(\bar{\mathbf{x}}), \bar{\mathbf{x}} = \mathbf{x} - \hat{\mathbf{x}}$. By exploiting the approximation of $Q(x)$ [Basar et al., 2013], we can express the unconditional PEP (UPEP) as

$$P(\mathbf{x} \to \hat{\mathbf{x}}) \cong E_{\mathbf{h}}\{(1/12)e^{-\frac{\Theta}{4N_0}} + (1/4)e^{\frac{\Theta}{3N_0}}\}. \tag{3.8}$$

Under the assumption $\mathbf{h} \sim \mathcal{CN}(0, \frac{1}{P}\mathbf{I}_P)$, the UPEP can be written as

$$P(\mathbf{x} \to \hat{\mathbf{x}}) = \frac{1/12}{\det(\frac{1}{P}\mathbf{I}_P + \alpha\mathbf{\Gamma}(\bar{\mathbf{x}}))} + \frac{1/4}{\det(\frac{1}{P}\mathbf{I}_P + \beta\mathbf{\Gamma}(\bar{\mathbf{x}}))} \tag{3.9}$$

where $\alpha = 1/4N_0$ and $\beta = 1/3N_0$. As $\mathbf{\Gamma}(\bar{\mathbf{x}})$ is a Hermitian matrix, the ith nonzero eigenvalue of $\mathbf{\Gamma}(\bar{\mathbf{x}})$ can be described as $\lambda_i, i \in \{1, \ldots, r\}$, where $r = \mathrm{rank}(\mathbf{\Gamma}(\bar{\mathbf{x}}))$. As mentioned in [Li et al., 2021], the coding gain depends on λ_i values and there is a relation between λ_i and the SMED of $\bar{\mathbf{x}}$ as $\sum_{i=1}^{r} \lambda_i = Pd_{\min}^2$.

Using the above analysis, we can express the average FER of the AEE-OTFS as follows

$$P_e \approx \frac{1}{|\mathcal{X}|} \sum_{\mathbf{x}} \sum_{\hat{\mathbf{x}} \neq \mathbf{x}} P(\mathbf{x} \rightarrow \hat{\mathbf{x}}). \tag{3.10}$$

3.3 Simulation Results And Comparisons

In this section, the FER performance of the AEE-OTFS scheme is evaluated via computer simulations. In all simulations, we define SNR as $\gamma = 1/N_0$ and assume that CSI is available at the receiver and the carrier frequency is $f_c = 4$ GHz. Each delay path in all simulations except theoretical results has a single Doppler shift generated with Jakes' model $\nu_i = \nu_{\max} \cos(\theta_i)$, where $\nu_{\max}$ corresponds to the maximum Doppler shift depending on the receiver speed and θ_i is uniformly distributed over $[-\pi, \pi]$. The receiver speed is taken as 506 km/h, which corresponds to $\nu_{\max} = 1875$ kHz. For the encoder and decoder NNs of the proposed AE, we consider one input, one hidden, and one output layer. For training, hyperparameters are selected such that SMED is maximized by exploiting a manual search method. The number of hidden units is selected as 128. Epoch, batch size, and learning rate are selected as 10^3, 512, and 0.0001, respectively, and varying ρ values have been exploited. ML detector is used for conventional OTFS system while LD is used for AEE-OTFS.

In Fig. 3.3, we compare computer simulation results for SE values of 1 and 2 bits/s/Hz with the upper bound FER curves obtained by (3.10). In these simulations, an ML detector is used and the selected system parameters are $M = N = 2$, $n = 2$, subcarrier spacing $\Delta f = 3.75$ kHz, and $P = 2$ with delay-Doppler profile $(l_i, k_i) = [(0,0)(1,1)]$, $i = 1, 2$. As seen from Fig. 3.3, it is shown that theoretical upper bounds and computer simulation results coincide with each other in the high SNR region.

In Fig. 3.4(a), error performance results are presented for different training SNR ρ values. The system parameters are specified as $M = N = 4$, $n = 4$, and $\Delta f = 3.75$ kHz. For the channel, we consider $P = 4$ taps with the maximum delay tap defined

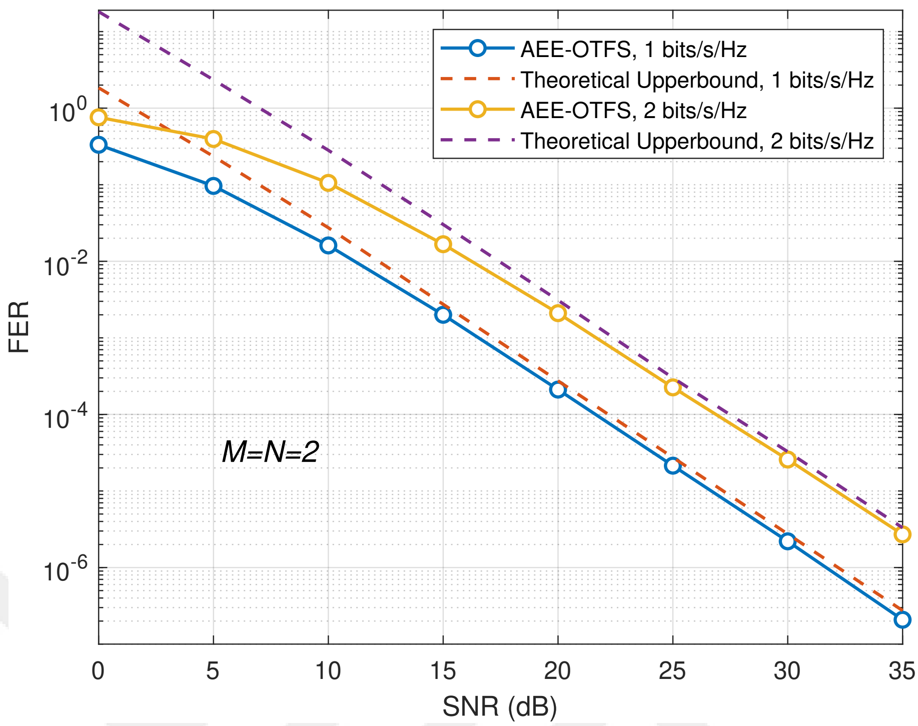

Figure 3.3: Average FER performance of AEE-OTFS scheme for SE values of 1 and 2 bits/s/Hz and $\rho = 5$ dB.

Table 3.1: SMED comparison of conventional PSK and AEE-OTFS.

	PSK	AEE-OTFS			
		$n = 2$	$n = 3$	$n = 4$	$n = 5$
1 bits/s/Hz	4	5.2277	5.6127	6.4352	7.0640
2 bits/s/Hz	2	2.2550	2.3858	2.5767	2.6803

as $l_{\max} = 3$, and the delay profile is given as $l_i = [0, 1, 2, 3]$. Note that BPSK and QPSK modulations are implemented for the conventional OTFS system to achieve 1 and 2 bits/s/Hz SE values. As seen from Fig. 3.4(a), the optimum training SNR ρ value can be selected as 5 dB. Additionally, at a FER value of 10^{-2}, AEE-OTFS provides a 2.6 dB gain over the classical OTFS for a SE value of 1 bits/s/Hz.

In Fig. 3.4(b), the FER performance of AEE-OTFS is compared to conventional OTFS system for varying block sizes n. The simulation parameters are the same as those used in Fig. 3.4(a). Note that the SE value equals 1.875 bits/s/Hz for

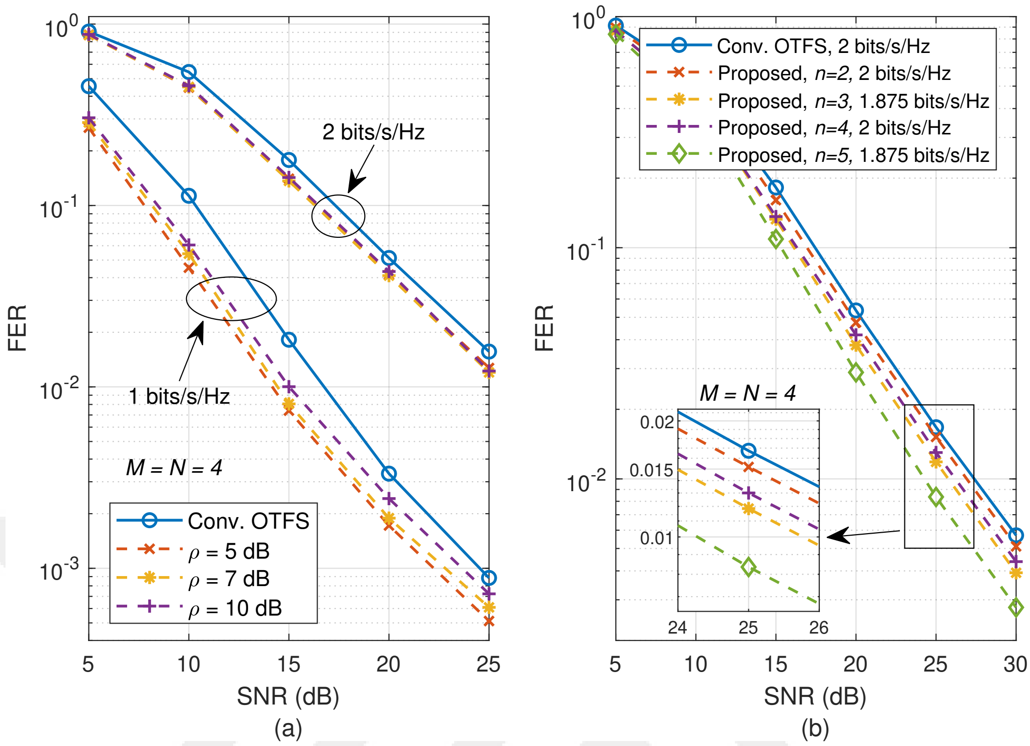

Figure 3.4: FER performance comparison of AEE-OTFS scheme using LD for (a) varying ρ with $n = 4$ and (b) varying n with $\rho = 5$ dB.

$n = 3$ and $n = 5$ since the frame size ($M \times N = 16$) is not an integer multiple of 3 and 5. Therefore, we apply zero-padding for $n = 3$ and $n = 5$. As seen from Fig. 3.4(b), the AEE-OTFS outperforms the conventional OTFS for all values of n. Moreover, AEE-OTFS with $n = 5$ performs better than other parameters. The superiority of the AEE-OTFS technique over OTFS in terms of error performance can be explained by the greater SMED values offered by the proposed method, as shown in Table 3.1.

In Fig. 3.5, the FER performance of AEE-OTFS is compared to OFDM and OTFS systems for a larger frame size, $M = N = 32$. Extended Vehicular A (EVA) channel model [ETSI TS 136 104 V14.3.0, 2017] is used. The subcarrier spacing Δf is 15 kHz. As seen from Fig. 3.5, at a FER value of 10^{-3}, AEE-OTFS approximately provides 2.8 and 1.9 dB gains over classical OTFS for 1 and 2 bits/s/Hz, respectively. Similarly, LD provides the same FER performance as that of ML

Table 3.2: The Complexity Comparison of Different Detectors for Different Frame Sizes and Block Sizes.

	OTFS, ML	AEE-OTFS, ML		AEE-OTFS, LD	
		$n = 2$	$n = 4$	$n = 2$	$n = 4$
$M = N = 16$	13.9	86.4	173.2	1.39	2.8
$M = N = 32$	59.4	322.18	641.24	2.95	5.9

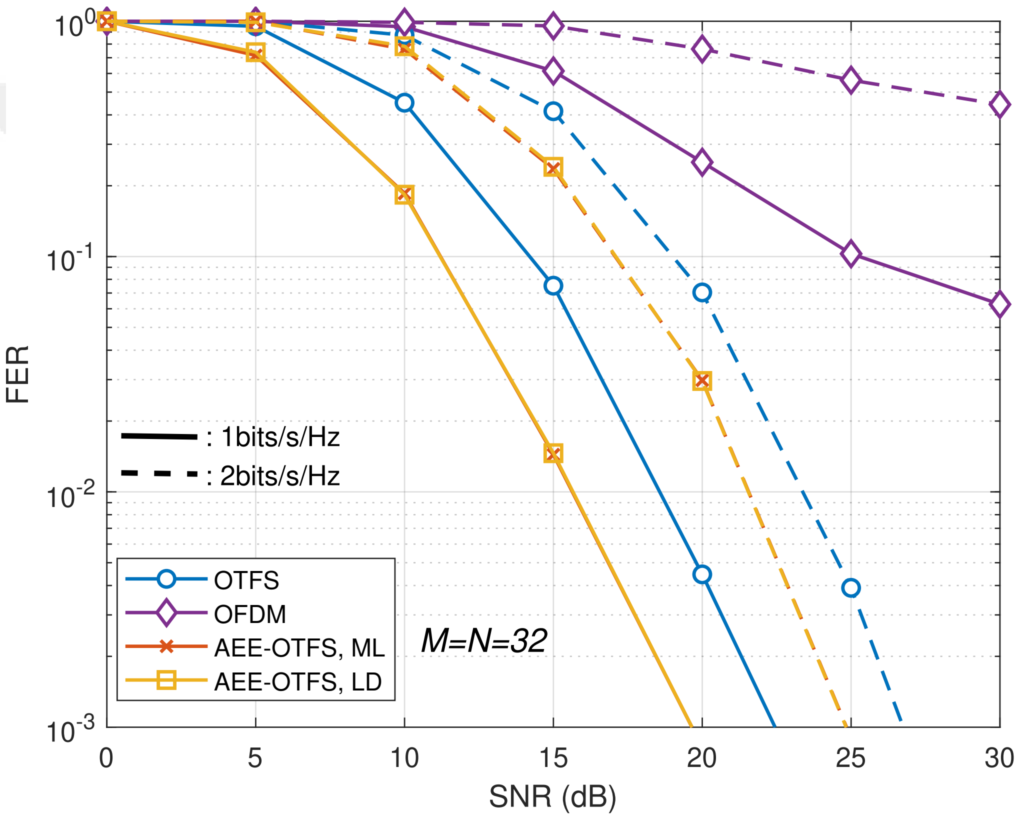

Figure 3.5: FER performance comparison of AEE-OTFS scheme for $M = N = 32$ with $n = 4$, SE values of 1 and 2 bits/s/Hz, and $\rho = 5$ dB.

detector. To investigate the decoding complexity of AEE-OTFS and OTFS, we calculated runtime in milliseconds. As seen from Table II, although AEE-OTFS with ML detector is more complex than classical OTFS with ML, it provides better error performance. Additionally, LD reduces the complexity significantly compared to the ML detector. Another important finding is that the complexity of AEE-OTFS with

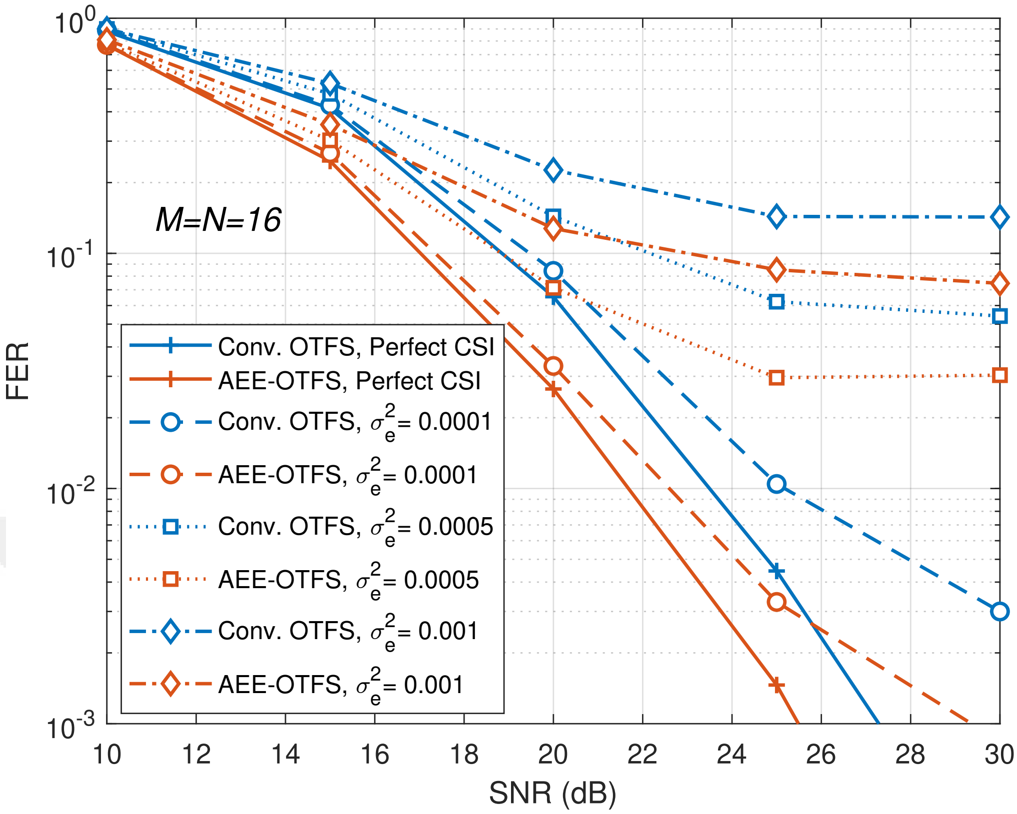

Figure 3.6: FER performance comparison of AEE-OTFS scheme using LD with conventional OTFS for $M = N = 16$ with $n = 4$, SE value of 2 bits/s/Hz, $\rho = 5$ dB, and $\Delta f = 15$ kHz under imperfect CSI.

LD is considerably less than classical OTFS with ML detector. Also, note that for larger n values, the number of n-dim symbols $|\mathcal{X}|$ increases. Consequently, decoding complexity also increases.

In Fig. 3.6, we investigate the error performance of AEE-OTFS under imperfect CSI and compare it with the conventional OTFS. As in [Raviteja et al., 2018], $\tilde{h}_i$ is exploited instead of h_i to model the channel estimation error, where $\tilde{h}_i = h_i + \epsilon$, $i = 1, \cdots, P$, and $\epsilon \sim \mathcal{CN}(0, \sigma_e^2)$. As seen from Fig. 3.6, AEE-OTFS outperforms the classical OTFS regarding error performance for different values of σ_e^2. As a result, the proposed scheme is more robust to channel estimation errors compared to the classical OTFS.

Chapter 4

JOINT DELAY-DOPPLER INDEX MODULATION FOR ORTHOGONAL TIME FREQUENCY SPACE MODULATION

Spreading information symbols across the entire delay-Doppler plane enables OTFS to achieve full diversity. Nevertheless, there is a need for enhanced reliability in OTFS systems to satisfy the rigorous requirements of forthcoming communication systems. To address this issue, we propose a scheme called JDDIM-OTFS. This scheme activates delay or Doppler resource elements in a subframe, and in order to obtain higher SE, we use different constellations for each active resource block. Furthermore, we utilize a low-complex detector with the help of a greedy approach.

In this chapter, the system model, performance analysis, and simulation results of JDDIM-OTFS are given.

4.1 System Model of JDDIM-OTFS

In this section, we describe the transceiver scheme of the proposed JDDIM-OTFS system and the modified MFGS detector.

4.1.1 Transmission of JDDIM-OTFS

We consider a ZP-based JDDIM-OTFS transmission system with a bandwidth of $M\Delta f$ and a total frame duration of NT, where $M, N, \Delta f$, and T are the number of subcarriers, number of symbols, subcarrier spacing, and symbol duration, respectively. The transceiver diagram is given in Fig. 4.1. We describe the L_{zp} as the length of ZP; hence, the number of data subcarriers is $M_{\mathrm{d}} = M - L_{\mathrm{zp}}$. Dissimilar to delay-IM (DeIM-OTFS)/Doppler-IM (DoIM-OTFS) schemes [Qian et al., 2023], our proposed JDDIM-OTFS scheme activates delay or Doppler re-

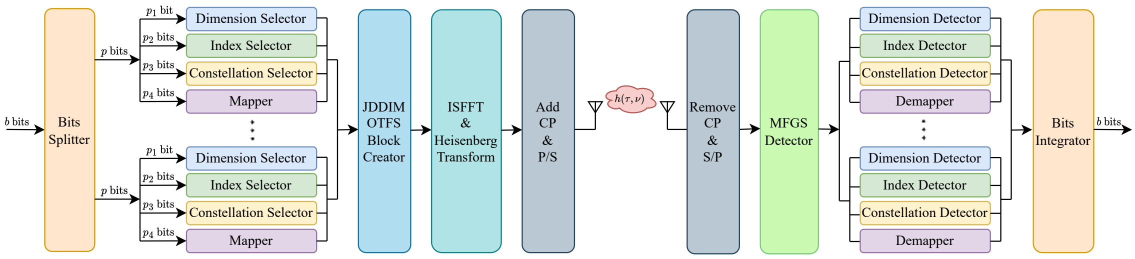

Figure 4.1: Transceiver scheme of JDDIM-OTFS system.

source blocks in a subframe as seen in Fig. 4.3. Furthermore, we choose different constellations for transmission through an activated resource block. The JDDIM-OTFS frame consists of G subframes, where $G = M_{\mathrm{d}}N/n$. We denote a subframe as $\mathbf{W}^g = [\mathbf{w}_1^g, \ldots, \mathbf{w}_n^g]^{\mathrm{T}} \in \mathbb{C}^{n\times n}$, where $\mathbf{w}_\varphi^g \in \mathbb{C}^{1\times n}$ is the φ-th row of $\mathbf{W}_g$, $\varphi = 1, \ldots, n$, and $g = 1, \ldots, G$. Assume a total number of b bits enter the system. Each subframe has k active resource blocks, and $p = b/G$ bits are processed in a subframe. These p information bits are divided into four parts:

1) $p_1 = \log_2(2) = 1$ bit decides the dimension of the resource blocks, where 2 is the number of dimensions (delay and Doppler dimensions). A subframe can contain only delay dimensional (i.e., active resource elements are in the columns of the subframe) or Doppler dimensional (i.e., active resource elements are in the rows of the subframe) resource blocks.

2) $p_2 = \lfloor \log_2(\mathrm{C}(n,k)) \rfloor$ bits are used to determine active resource block indices $\mathcal{I}^g = \{i_1^g, \ldots, i_k^g\}$ for $i_\beta^g \in [1, \ldots, n]$ and $\beta = 1, \ldots, k$. Each subframe has only nk resource elements, and there are $\mathrm{C}(n,k)$ possible index combinations.

3) For each activated resource block, the $p_3 = k\lfloor \log_2(n_{\mathrm{c}}) \rfloor$ bits select the constellation indices $\mathcal{C}^g = \{c_1^g, \ldots, c_k^g\}$ for $c_\kappa^g \in [1, \ldots, n_{\mathrm{c}}]$ and $\kappa = 1, \ldots, k$, where n_{c} is the number of different constellations and constellation sets are given as $\mathcal{M} = \{\mathcal{M}_1, \ldots, \mathcal{M}_{n_{\mathrm{c}}}\}$. Some example constellations can be seen in Fig. 4.2.

4) Lastly, the $p_4 = nk\log_2(Q)$ bits are mapped to the corresponding constellation symbols, where Q is the modulation order. In order to map bits to symbols, the p_4 bits are arranged into a $k \times n\log_2(Q)$ bit matrix. The bits in the ρ-th row of this matrix belong to ρ-th active resource block and are mapped with $\mathcal{M}_{c_\rho^g}$, $\rho = 1, \ldots, k$.

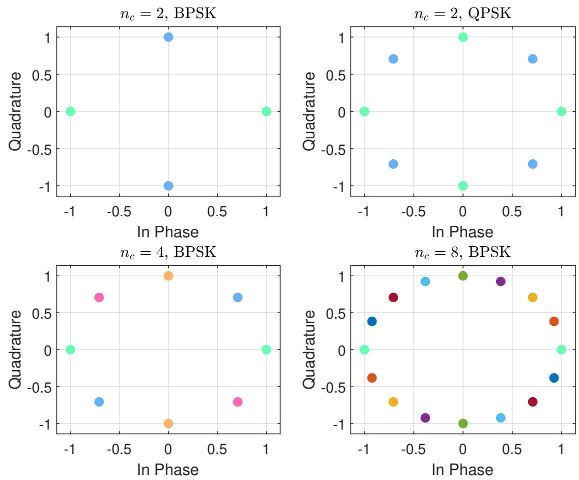

Figure 4.2: Different constellation examples.

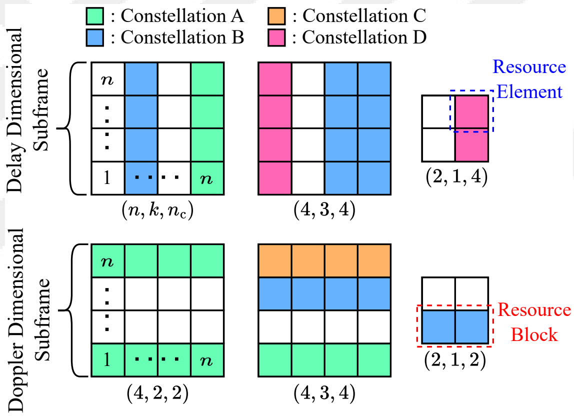

Figure 4.3: JDDIM-OTFS subframe structure.

The mapped symbols can be represented as $\mathbf{Q}^g = [\mathbf{q}_1^g, \ldots, \mathbf{q}_k^g]^{\mathrm{T}} \in \mathbb{C}^{k \times n}$ where $\mathbf{q}_\phi^g \in \mathbb{C}^{1 \times n}$ and $\phi = 1, \ldots, k$.

After mapping, symbols are placed in k active resource blocks of g-th subframe as $\mathbf{w}_{i_\phi^g}^g = \mathbf{q}_\phi^g$. The remaining resource elements in the $\mathbf{W}^g$ are set to zero. According to the dimension bit, the structure of the subframe is determined. If the dimension bit is 0, a transpose operation is performed to $\mathbf{W}^g$ in order to make it delay dimensional; otherwise, for dimension bit 1, $\mathbf{W}^g$ is used without a change. The example subframe structures are illustrated in Fig. 4.3. The total number of transmitted bits with a JDDIM-OTFS frame is given by $Gp = G(p_1 + p_2 + p_3 + p_4)$. The SE of the

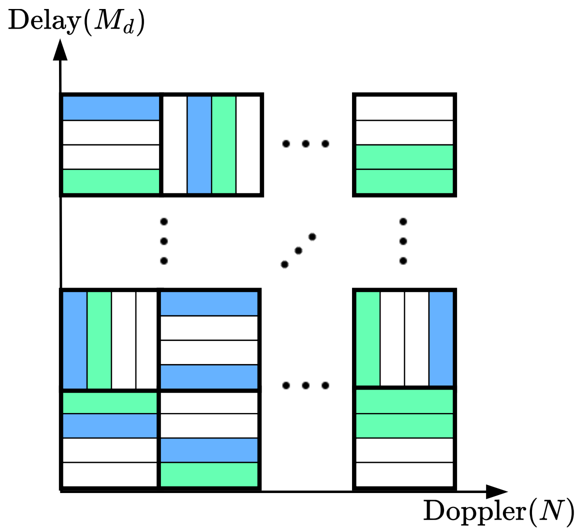

Figure 4.4: A exemplary JDDIM-OTFS data frame.

JDDIM-OTFS system can be calculated as p/n^2 bits/s/Hz.

After generating subframes as $\{\mathbf{W}^1, \ldots, \mathbf{W}^G\}$, the delay-Doppler domain data signal $\mathbf{X}_\mathrm{d} \in \mathbb{C}^{M_\mathrm{d} \times N}$ is obtained by placing subframes into the grid. Then, the $\mathbf{0}_{N \times L_\mathrm{zp}}$ guard samples are inserted below the $\mathbf{X}_\mathrm{d}$ and the delay-Doppler domain transmit signal $\mathbf{X} \in \mathbb{C}^{M \times N}$ is obtained as $\mathbf{X} = [\mathbf{X}_\mathrm{d}\ \mathbf{0}_{N \times L_\mathrm{zp}}]^\mathrm{T}$.

For transmission, the time-domain transmit signal $\mathbf{S}$ can be obtained by converting $\mathbf{X}$ into the time-frequency domain by implementing ISFFT and performing the Heisenberg transform assuming ideal pulses (i.e., $\mathbf{G}_\mathrm{tx} = \mathbf{I}_M$), as given in the following equation

$$\mathbf{S} = \mathbf{G}_\mathrm{tx}\mathbf{F}_M^\mathrm{H}(\mathbf{F}_M\mathbf{X}\mathbf{F}_N^\mathrm{H}) = \mathbf{I}_M\mathbf{X}\mathbf{F}_N^\mathrm{H} = \mathbf{X}\mathbf{F}_N^\mathrm{H}. \tag{4.1}$$

In the next step, time-domain transmit vector $\mathbf{s} \in \mathbb{C}^{MN \times 1}$ is obtained by applying column-wise vectorization to $\mathbf{S}$, and a cyclic prefix is added to $\mathbf{s}$ in order to avoid inter-symbol interference. Then, $\mathbf{s}$ is obtained at the receiver over a doubly-dispersive channel. The channel impulse response of the doubly-dispersive channel is given by $h(\tau, \nu) = \sum_{i=1}^{P} h_i \delta(\tau - \tau_i)\delta(\nu - \nu_i)$, where P is the number of propagation paths, h_i, τ_i and ν_i stand for the complex channel gain, delay shift, and Doppler shift for the ith path, respectively.

At the receiver, after removing CP, the received time domain signal can be expressed as $\mathbf{r} = \mathbf{H}\mathbf{s} + \mathbf{w}$, where $\mathbf{w} \in \mathbb{C}^{MN\times 1}$ is a vector of zero mean AWGN samples with $\mathcal{CN}(0, N_0\mathbf{I}_{MN})$, N_0 is the noise variance, and $\mathbf{H} \in \mathbb{C}^{MN\times MN}$ is the time domain channel matrix given by

$$\mathbf{H} = \sum_{i=1}^{P} h_i \mathbf{\Pi}^{l_i} \mathbf{\Delta}^{k_i}, \tag{4.2}$$

where $\mathbf{\Pi}$ is the forward cyclic shift matrix and $\mathbf{\Delta} = \mathrm{diag}[z^0, z^1, \ldots, z^{MN-1}] \in \mathbb{C}^{MN\times MN}$ with $z \triangleq e^{-2\pi j/MN}$ represents the diagonal Doppler shift matrix. We define the fading parameters for the ith path as $h_i \sim \mathcal{CN}(0, 1/P)$, $l_i = \tau_i M\Delta f$ and $k_i = \nu_i NT$ where l_i and k_i represent delay taps and Doppler taps, respectively.

After the signal is received, $\mathbf{r}$ is sent to the MFGS detector to decode the corresponding information bits.

4.1.2 Iterative MFGS Detector

In this section, we explain the MFGS detector combined with the ML and greedy detectors. As mentioned in [Thaj et al., 2021], thanks to time domain ZP, time domain inter-block interference is averted. Thus, the time domain input-output relation can be split and independently processed block-wise as

$$\mathbf{r}_\eta = \mathbf{H}_\eta \mathbf{s}_\eta + \mathbf{w}_\eta, \quad \eta = 0, \ldots, N-1, \tag{4.3}$$

where $\mathbf{H}_\eta \in \mathbb{C}^{M\times M}$ and $\mathbf{w}_\eta \in \mathbb{C}^{M\times 1}$ are the time domain channel matrix and the zero mean AWGN samples for η-th symbol.

In this detector, the iterations use match-filtered channel blocks $\mathbf{R}_\eta = \mathbf{H}_\eta^{\mathrm{T}}\mathbf{H}_\eta$. After performing the match-filtering procedure, the input-output relation in (4.3) can be expressed as

$$\mathbf{z}_\eta = \mathbf{R}_\eta \mathbf{s}_\eta + \bar{\mathbf{w}}_\eta, \tag{4.4}$$

where $\mathbf{R}_\eta = \mathbf{H}_\eta^{\mathrm{H}}\mathbf{H}_\eta$, $\mathbf{z}_\eta = \mathbf{H}_\eta^{\mathrm{H}}\mathbf{r}_\eta$ and $\bar{\mathbf{w}}_\eta = \mathbf{H}_\eta^{\mathrm{H}}\mathbf{w}_\eta$. The aim of the iterative MFGS detector is to find the least squares solution $\hat{\mathbf{s}} = \min \|\mathbf{z}_\eta - \mathbf{R}_\eta \mathbf{s}_\eta\|^2$ of the M-dimensional linear system of equations in (4.4). Consider matrices $\mathbf{D}_\eta$ and $\mathbf{L}_\eta$, where $\mathbf{D}_\eta$ contains the elements along the main diagonal of $\mathbf{R}_\eta$, and $\mathbf{L}_\eta$ contains the elements in the lower triangular portion of $\mathbf{R}_\eta$, excluding the diagonal. The each iteration step of the MFGS method to estimate $\mathbf{s}_\eta$ is expressed as

$$\hat{\mathbf{s}}_\eta^{(i)} = -\mathbf{T}_\eta \hat{\mathbf{s}}_\eta^{(i-1)} + \mathbf{b}_\eta, \tag{4.5}$$

$$\mathbf{T}_\eta = (\mathbf{D}_\eta + \mathbf{L}_\eta)^{-1}\mathbf{L}_\eta^{\mathrm{H}}, \;\; \mathbf{b}_\eta = (\mathbf{D}_\eta + \mathbf{L}_\eta)^{-1}\mathbf{z}_\eta, \tag{4.6}$$

where $\mathbf{T}_\eta$ represents the GS iteration matrix and $\hat{\mathbf{s}}_\eta^{(i)}$ stands for the estimated time domain samples of η-th symbol block of $\mathbf{S}$. The delay-Doppler domain information symbols in the i-th iteration are given as

$$\hat{\mathbf{X}}^{(i)} = \mathcal{D}(\tilde{\mathbf{X}}^{(i)}), \;\; \tilde{\mathbf{X}}^{(i)} = \hat{\mathbf{S}}^{(i)}\mathbf{F}_N, \tag{4.7}$$

where $\hat{\mathbf{S}}^{(i)} = [\hat{\mathbf{s}}_0^{(i)}, \ldots, \hat{\mathbf{s}}_N^{(i)}]$ and $\mathcal{D}(\cdot)$ is the decision making function. In a conventional MFGS detector, $\mathcal{D}(\cdot)$ replaces all estimated information symbols with the nearest QAM/PSK symbol. However, we do not replace the nearest QAM/PSK symbols in this study. Instead, we split $\tilde{\mathbf{X}}^{(i)}$ into subframes as $\{\tilde{\mathbf{W}}^1, \ldots, \tilde{\mathbf{W}}^G\}$ and we replace them with detected subframes by using an ML or greedy detector.

MFGS-ML Detector

The ML detector compares $\tilde{\mathbf{W}}^g$ with all possible $C = 2^p$ subframe realizations. It selects the subframe that is most probable to have been transmitted based on the received signal, and for the next iteration step, $\hat{\mathbf{X}}^{(i)}$ is obtained by placing selected subframes and ZP parts into the grid.

MFGS-GRD Detector

In this greedy detector approach, first, we detect the active resource blocks and the direction of related resource blocks by considering the total energy of each row and column. Afterward, we determine the QAM/PSK symbols independently in the active resource blocks and replace them with the nearest symbols. The details are as follows.

Step 1: Let us define $\mathbf{\Theta}_{\mathrm{r}}^g = [\Theta_{\mathrm{r}_1}^g, \ldots, \Theta_{\mathrm{r}_n}^g]$ and $\mathbf{\Theta}_{\mathrm{c}}^g = [\Theta_{\mathrm{c}_1}^g, \ldots, \Theta_{\mathrm{c}_n}^g]$ are the total energy vector of each row and column of the g-th received subframe $\tilde{\mathbf{W}}^g$, respectively.

$\boldsymbol{\Theta}_{\mathrm{r}}^{g}$ and $\boldsymbol{\Theta}_{\mathrm{c}}^{g}$ can be calculated as follows

$$\Theta_{\mathrm{r}_\alpha}^{g} = \sum_{\mu=1}^{n} |\tilde{\mathbf{W}}^{g}(\alpha, \mu)|^2, \tag{4.8}$$

$$\Theta_{\mathrm{c}_\alpha}^{g} = \sum_{\mu=1}^{n} |\tilde{\mathbf{W}}^{g}(\mu, \alpha)|^2, \tag{4.9}$$

where $\alpha = 1, \ldots, n$ and $g = 1, \ldots, G$.

Step 2: In order to decide whether the subframe is delay dimensional or Doppler dimensional, the norms of $\boldsymbol{\Theta}_{\mathrm{r}}^{g}$ and $\boldsymbol{\Theta}_{\mathrm{c}}^{g}$ are compared. If $\|\boldsymbol{\Theta}_{\mathrm{c}}^{g}\| > \|\boldsymbol{\Theta}_{\mathrm{r}}^{g}\|$, the subframe is delay dimensional otherwise, the subframe is Doppler dimensional. After, by considering the dimension of the subframe, the set of active resource block indices $\hat{\mathcal{I}}^{g} = \{\hat{i}_0^{g}, \ldots, \hat{i}_k^{g}\}$ can be detected by finding the indices of k elements of $\boldsymbol{\Theta}_{g}^{\mathrm{r}}$ or $\boldsymbol{\Theta}_{g}^{\mathrm{c}}$ with highest energy.

Step 3: Let $\tilde{\mathbf{Q}}^{g} = [\tilde{\mathbf{q}}_1^{g}, \ldots, \tilde{\mathbf{q}}_k^{g}]^{\mathrm{T}} \in \mathbb{C}^{k\times n}$ be the received information symbols in $\tilde{\mathbf{W}}^{g}$. The received information symbols in the active resource blocks are replaced individually with the nearest QAM/PSK symbols, considering all $\mathcal{M}$, as

$$\tilde{\mathbf{Q}}^{g}(\upsilon, \varsigma) \leftarrow \underset{\mathcal{S}(t)_\psi \in \mathcal{M}_\psi}{\arg\min} \|\tilde{\mathbf{Q}}^{g}(\upsilon, \varsigma) - \mathcal{S}(t)_\psi\|^2, \tag{4.10}$$

where $\upsilon = 1, \ldots, k$, $\varsigma = 1, \ldots, n$, $t = 1, \ldots, Q$ and $\psi = 1, \ldots, n_{\mathrm{c}}$.

Step 4: Afterward, $\tilde{\mathbf{W}}^{g}$ is recreated by placing symbols of $\tilde{\mathbf{Q}}^{g}$ according to $\hat{I}^{g}$ and decided dimension similar to what is explained in Section II.

Step 5: For the next iteration step, $\hat{\mathbf{X}}^{(i)}$ is obtained by placing recreated subframes and ZP parts into the grid.

After using ML or greedy detector, $\hat{\mathbf{X}}^{(i)}$ is converted into the time domain back in order to update the time domain estimate for use in the subsequent iteration.

$$\hat{\mathbf{s}}^{(i)} \leftarrow (1-\omega)\hat{\mathbf{s}}^{(i)} + \omega \mathrm{vec}(\hat{\mathbf{X}}^{(i)}\mathbf{F}_N), \tag{4.11}$$

where ω is the relaxation parameter. $\hat{\mathbf{X}}^{(0)} = \mathbf{0}_{M\times N}$ is chosen for the initial estimate.

4.2 Detector Complexity

As indicated in [Thaj and Viterbo, 2020], the number of complex multiplications for initial computations of $\mathbf{R}_\eta, \mathbf{b}_\eta$ and $\mathbf{T}_\eta$ is $O(NML)$, where L represents the count of distinct delay taps and is usually considerably smaller than P. In this work, the initial computation complexity is still same. In terms of the complexity per iteration, a conventional MFGS detector has $NM^2+N^2M_{\mathrm{d}}+NM_{\mathrm{d}}Q$. In an iteration, every subframe has to be checked and replaced. In the case of using an MFGS-ML detector, there are C possible subframe realizations and G subframe. As a result, the complexity becomes $NM^2 + N^2M_{\mathrm{d}} + GCn^2$. For the MFGS-GRD detector, there are n^2 energy calculation operations and nk information symbol detections. Consequently, the complexity becomes $NM^2 + N^2M_{\mathrm{d}} + Gn(n + Qn_{\mathrm{c}}k)$.

4.3 Performance Analysis

In this section, for the JDDIM-OTFS, we obtain an upper bound on the bit error rate (BER) by using ML detection.

The received signal in the delay-Doppler domain can be expressed as

$$\begin{aligned}
\mathbf{y} &= \mathbf{H}_{\mathrm{eff}}\mathbf{x} + \tilde{\mathbf{w}} \\
\mathbf{y} &= \sum_{i=1}^{P} h_i(\mathbf{I}_M \otimes \mathbf{F}_N)(\mathbf{P}^{\mathrm{T}}\mathbf{\Pi}^{l_i}\mathbf{\Delta}^{k_i}\mathbf{P})(\mathbf{I}_M \otimes \mathbf{F}_N^{\mathrm{H}})\mathbf{x} + \tilde{\mathbf{w}} \\
&= \mathbf{\Phi}(\mathbf{x})\mathbf{h} + \tilde{\mathbf{w}}, \qquad (4.12)
\end{aligned}$$

where $\mathbf{h} = [h_1, h_2, \ldots, h_P]^{\mathrm{T}} \in \mathbb{C}^{P\times 1}$ is the vector of channel coefficients, $\mathbf{P}$ is the row-column interleaver matrix [Thaj et al., 2021], $\mathbf{x}$ is the columns-wise vectorized version of $\mathbf{X}^{\mathrm{T}}$, $\tilde{\mathbf{w}} = (\mathbf{I}_M \otimes \mathbf{F}^{\mathrm{H}})(\mathbf{P}^{\mathrm{T}}\mathbf{w})$ is the delay-Doppler domain noise samples and $\mathbf{\Phi}(\mathbf{x}) \in \mathbb{C}^{MN\times P}$ is a concatenated matrix given by

$$\mathbf{\Phi}(\mathbf{x}) = [\mathbf{\Psi}_1\mathbf{x}, \mathbf{\Psi}_2\mathbf{x}, \ldots, \mathbf{\Psi}_P\mathbf{x}], \qquad (4.13)$$

$$\mathbf{\Psi}_i \triangleq (\mathbf{I}_M \otimes \mathbf{F}_N)(\mathbf{P}^{\mathrm{T}}\mathbf{\Pi}^{l_i}\mathbf{\Delta}^{k_i}\mathbf{P})(\mathbf{I}_M \otimes \mathbf{F}_N^{\mathrm{H}}). \qquad (4.14)$$

We assume that perfect CSI is available at the receiver. Let us define the error vector as $\bar{\mathbf{x}} = \mathbf{x} - \hat{\mathbf{x}}$ when $\mathbf{x}$ is transmitted and erroneously detected $\hat{\mathbf{x}}$. We can express the conditional Euclidean distance $\delta_{\bar{\mathbf{x}}}$ of this event as

$$\delta_{\bar{\mathbf{x}}} = \|\mathbf{\Phi}(\bar{\mathbf{x}})\mathbf{h}\|^2 = \mathbf{h}^{\mathrm{H}}\mathbf{\Omega}\mathbf{h}, \qquad (4.15)$$

where $\Omega = \mathbf{\Phi}(\bar{\mathbf{x}})^{\mathrm{H}}\mathbf{\Phi}(\bar{\mathbf{x}})$. We can express the unconditional PEP (UPEP) as

$$P(\mathbf{x} \rightarrow \hat{\mathbf{x}}) = P(\|\mathbf{y} - \mathbf{\Phi}(\hat{\mathbf{x}})\mathbf{h}\|^2 \leq \|\mathbf{y} - \mathbf{\Phi}(\mathbf{x})\mathbf{h}\|^2) \ . \tag{4.16}$$

After some mathematical simplifications and rearrangements, (4.16) can be further simplified, and we can rewrite it as

$$P(\mathbf{x} \rightarrow \hat{\mathbf{x}}) = P\left(\Re\{\tilde{\mathbf{w}}^{\mathrm{H}}\mathbf{\Phi}(\bar{\mathbf{x}})\mathbf{h}\} \geq \frac{\|\mathbf{\Phi}(\bar{\mathbf{x}})\mathbf{h}\|^2}{2}\right). \tag{4.17}$$

From (4.17), it can be seen that $\Re\{\tilde{\mathbf{w}}^{\mathrm{H}}\mathbf{\Phi}(\bar{\mathbf{x}})\mathbf{h}\}$ follows Gaussian distribution with zero mean and a variance of $\|\mathbf{\Phi}(\bar{\mathbf{x}})\mathbf{h}\|N_0/2$. Hence, considering (4.15) and by exploiting the Chernoff bound, [Sui et al., 2023], the CPEP of (4.17) can be represented as

$$P(\mathbf{x} \rightarrow \hat{\mathbf{x}}) = Q\left(\sqrt{\frac{\delta_{\bar{\mathbf{x}}}}{2N_0}}\right) \leq \frac{1}{2}e^{\frac{-\delta_{\bar{\mathbf{x}}}}{4N_0}}. \tag{4.18}$$

As $\mathbf{\Omega}$ is a Hermitian matrix, the ith nonzero eigenvalue of $\mathbf{\Omega}$ can be described as $\lambda_i, i \in \{1, \ldots, r\}$ and the eigenvectors of $\mathbf{\Omega}$ can be given as $\{\mathbf{v_0}, \ldots, \mathbf{v_r}\}$ where $r = \mathrm{rank}(\mathbf{\Omega})$. Using the above analysis, the CPEP can be further upper-bounded as

$$P(\mathbf{x} \rightarrow \hat{\mathbf{x}}) \leq \frac{1}{2}\exp\left(-\frac{\sum_{i=1}^{r}\lambda_i|\bar{h}_i|^2}{4N_0}\right). \tag{4.19}$$

As mentioned in [Sui et al., 2023], $|\bar{h}_i|$ are Rician distributed. By averaging (4.19) with respect to $|\bar{h}_i|$, we can rewrite the UPEP as

$$P(\mathbf{x} \rightarrow \hat{\mathbf{x}}) \leq \frac{1}{2}\prod_{i=1}^{r}\frac{1}{1+\frac{\lambda_i}{4PN_0}}\exp\left(-\frac{\frac{\zeta_i\lambda_i}{4PN_0}}{1+\frac{\lambda_i}{4PN_0}}\right), \tag{4.20}$$

where ζ_i represents the Rician factor. Assuming $\zeta_i = 0$, $|\bar{h}_i|$ follows the Rayleigh distribution. Therefore, we can rearrange (4.20) as follows

$$P(\mathbf{x} \rightarrow \hat{\mathbf{x}}) \leq \frac{1}{\prod_{i=1}^{r} 1+\frac{\lambda_i}{4PN_0}}. \tag{4.21}$$

Ultimately, utilizing the approach of union bounding, an approximate expression for the BER of JDDIM-OTFS can be formulated as

$$P_e \approx \frac{1}{b2^b}\sum_{\mathbf{x}}\sum_{\hat{\mathbf{x}}\neq\mathbf{x}} P(\mathbf{x} \rightarrow \hat{\mathbf{x}})e(\mathbf{x}, \hat{\mathbf{x}}) \tag{4.22}$$

where $e(\mathbf{x}, \hat{\mathbf{x}})$ is the difference in number of information bits between $\mathbf{x}$ and $\hat{\mathbf{x}}$.

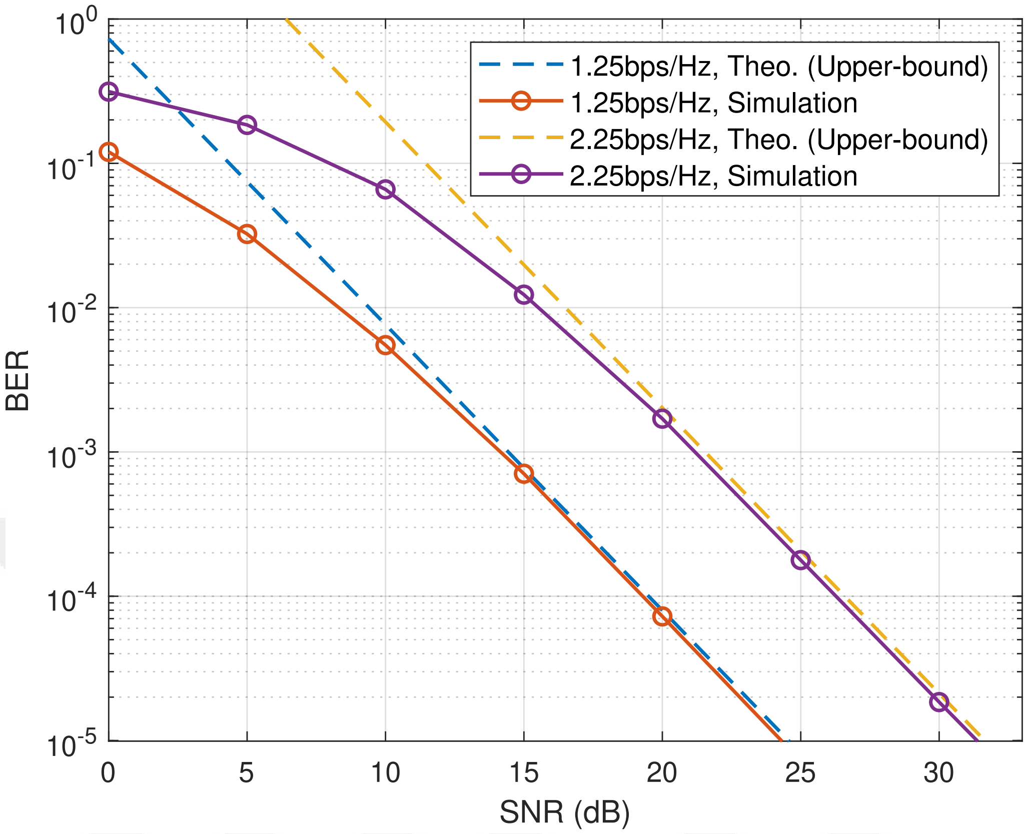

Figure 4.5: Average BER performance of JDDIM-OTFS scheme for SE values of 1.25 and 2.25 bits/s/Hz.

4.4 Simulation Results And Comparisons

In this section, the BER performance of the JDDIM-OTFS scheme is evaluated via computer simulations. In all simulations, we define SNR as $\gamma = 1/N_0$ and assume that CSI is available at the receiver and the carrier frequency is $f_c = 4$ GHz. Each delay path in all simulations except theoretical results has a single Doppler shift generated with Jakes' model $\nu_i = \nu_{\max} \cos(\theta_i)$, where $\nu_{\max}$ corresponds to the maximum Doppler shift depending on the receiver speed and θ_i is uniformly distributed over $[-\pi, \pi]$. The receiver speed is taken as 506 km/h, which corresponds to $\nu_{\max} = 1875$ kHz.

In Fig. 4.5, we compare computer simulation results for SE values of 1.25 and 2.25 bits/s/Hz with the upper bound BER curves obtained by (4.22). In these simulations, an ML detector is used and the selected system parameters are $M =$

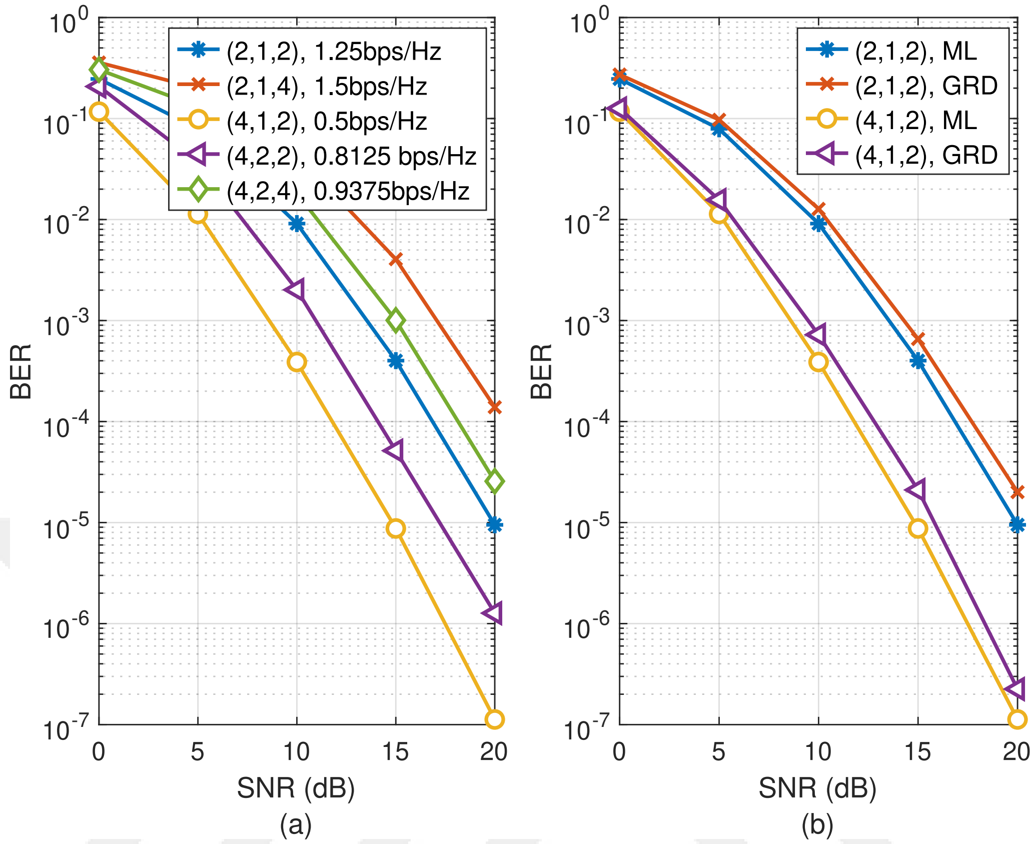

Figure 4.6: BER performance comparison of the JDDIM-OTFS scheme for (a) different subframe structures and (b) for ML and Greedy detectors.

$4, M_{\rm d} = N = 2$, $n = 2, k = 1, n_c = 2$, BPSK, subcarrier spacing $\Delta f = 3.75$ kHz, and $P = 2$ with delay-Doppler profile $(l_i, k_i) = [(0,0)(1,1)]$. Fig. 4.5 demonstrates that the theoretical upper limits align with the computer simulation outcomes in the high SNR region.

In Fig. 4.6(a), error performance results of JDDIM-OTFS are presented for different subframe parameters $(n, k, n_{\rm c})$, and in Fig. 4.6(b), MFGS-ML detector and MFGS-GRD detector are compared. In these simulations, $M = 8, M_{\rm d} = 4, N = 8$, subcarrier spacing $\Delta f = 15$ kHz, and $P = 4$ with delay profile $l_i = [0, 1, 2, 3]$ are selected as simulation parameters. As seen from Fig. 4.6(a), the $(4, 1, 2)$ scheme performs the best error performance. Furthermore, it can also be seen from the figure that while the k is increased, the BER performance degrades. This can be comprehended as the detection of data symbols and active resource block indices be-

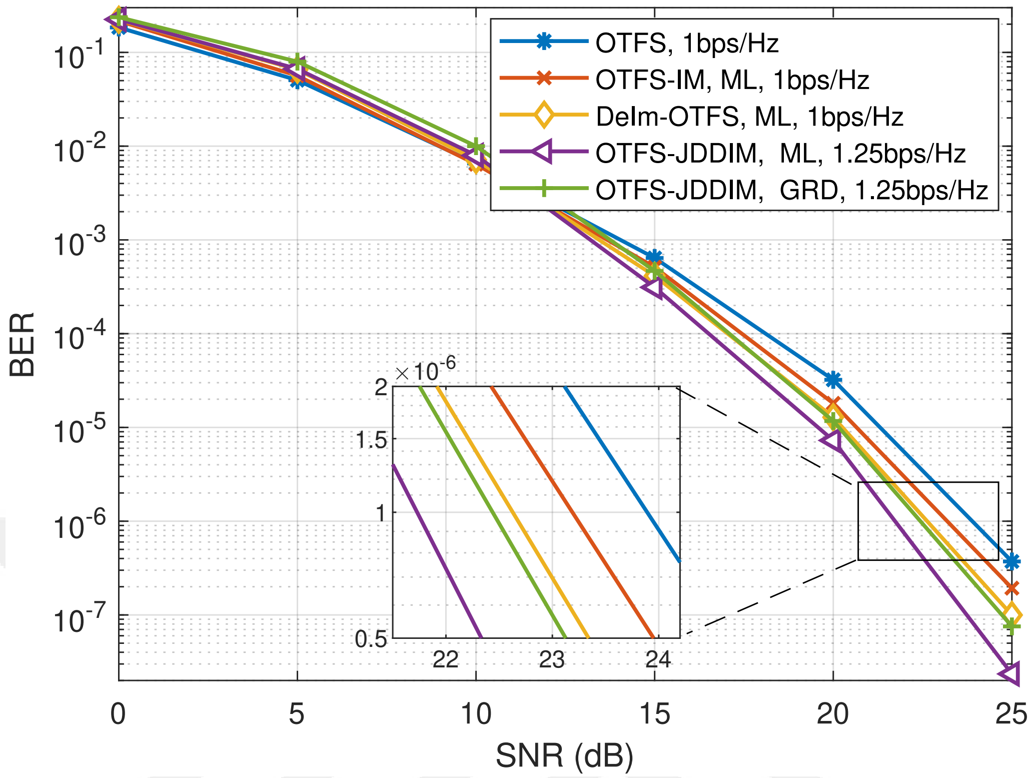

Figure 4.7: BER performance comparison of JDDIM-OTFS scheme using ML and Greedy detectors with other schemes for a SE 1.25bps/Hz value.

comes more demanding when aiming for higher SE due to the presence of significant interference. When Fig. 4.6(b) is examined, it can be seen that even though the MFGS-GRD detector has low complexity, the MFGS-ML detector exhibits better error performance than the MFGS-GRD detector and there is approximately 1 dB difference between them.

In Fig. 4.7, the BER performance of JDDIM-OTFS is compared to conventional OTFS, OTFS-IM, and DeIM-OTFS for 1.25 bits/s/Hz. The simulation parameters are selected as $M = 16, M_\mathrm{d} = 12, N = 16$. EVA model is used for channel delay profile. For the JDDIM-OTFS(n, k, n_c) scheme, the selected parameters are $(2, 1, 2)$, and BPSK modulation is used to reach 1.25 bits/s/Hz. We observe that the JDDIM-OTFS with MFGS-ML and MFGS-GRD detectors outperform all other schemes. At a BER level 10^{-6}, JDDIM-OTFS with MFGS-ML provides 2.1, 1.5, and 0.9 dB gain over OTFS, OTFS-IM, and DeIM-OTFS, respectively. When JDDIM-OTFS with

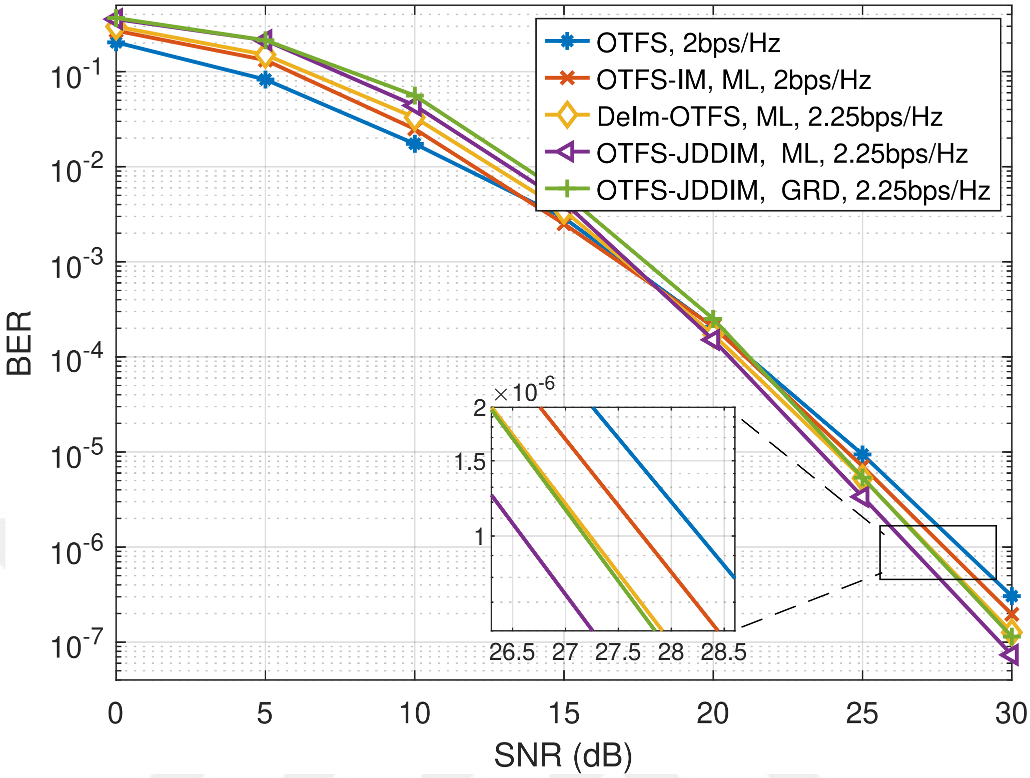

Figure 4.8: BER performance comparison of JDDIM-OTFS scheme using ML and Greedy detectors with other schemes for a SE 2.25bps/Hz value.

MFGS-GRD detector is examined, we can see a 0.7 dB difference between the MFGS-ML detector. Also, JDDIM-OTFS with MFGS-GRD detector provides 1.4, 0.8, and 0.2 dB gain over OTFS, OTFS-IM, and DeIM-OTFS, respectively. Both MFGS-ML and MFGS-GRD detectors provide a 25% higher SE as well as performance gain.

In Fig. 4.8, the BER performance of JDDIM-OTFS is compared to conventional OTFS, OTFS-IM, and DeIM-OTFS for 2.25 bits/s/Hz. The frame size and the channel delay profile are the same as those used in Fig. 4.7. For the JDDIM-OTFS(n, k, n_c) scheme, the selected parameters are $(2, 1, 2)$, and 8-PSK modulation is used to reach 2.25 bits/s/Hz. It is observed from Fig. 4.8 that the JDDIM-OTFS with MFGS-ML detector surpasses all alternative schemes in performance. At a BER level 10^{-6}, JDDIM-OTFS with MFGS-ML provides 1.66, 1.1, and 0.6 dB gain over OTFS, OTFS-IM, and DeIM-OTFS, respectively. When JDDIM-OTFS with MFGS-GRD detector is examined, we can see that the MFGS-GRD detector

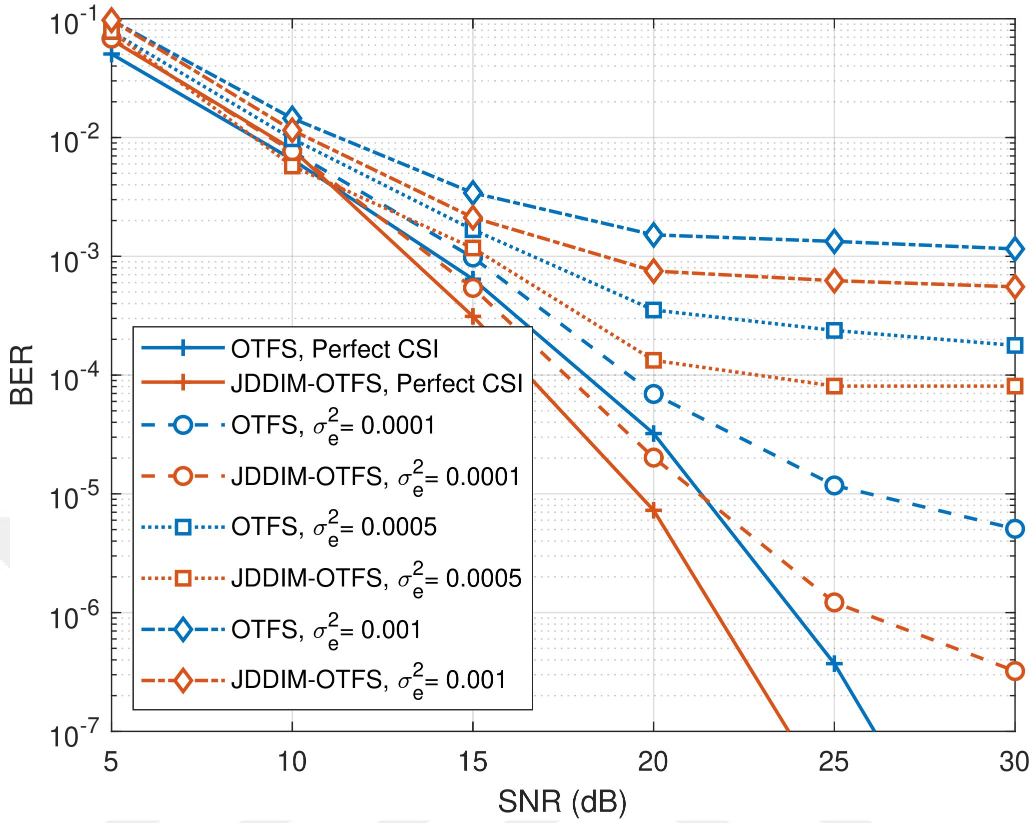

Figure 4.9: BER performance comparison of JDDIM-OTFS(2, 1, 2), BPSK scheme and conventional OTFS, BPSK under imperfect CSI for $M = 16, M_{\mathrm{d}} = 12, N = 16$.

exhibits nearly identical performance as DeIM-OTFS. Similar to the findings in the previous simulation results, both MFGS-ML and MFGS-GRD detectors yield a 12.5% increase in SE along with performance improvement.

In Fig. 4.9, we examine the error characteristics of JDDIM-OTFS when subjected to imperfect CSI and make a comparison with conventional OTFS. As in [Tek et al., 2023], we utilize $\tilde{h}_i$ instead of h_i to represent the channel estimation error, where $\tilde{h}_i = h_i + \epsilon$, $i = 1, \cdots, P$, and $\epsilon \sim \mathcal{CN}(0, \sigma_e^2)$. As seen from Fig. 4.9, JDDIM-OTFS demonstrates superior error performance compared to classical OTFS across various values of σ_e^2. Consequently, the proposed scheme exhibits greater resilience to channel estimation errors when compared to OTFS since the dimension bits and active resource block indices can still be recovered under imperfect CSI.

Chapter 5

PAPR REDUCTION PRECODING FOR ORTHOGONAL TIME FREQUENCY SPACE MODULATION

OTFS modulation is a promising technique for efficient data transmission in wireless communication systems, particularly in high-mobility scenarios. However, as in other multicarrier schemes, OTFS has one major drawback, high peak-to-average power ratio (PAPR), which can lead to signal distortion and performance degradation. There are various techniques to reduce the PAPR for multicarrier systems. One of these techniques is precoding. In multicarrier systems, precoders such as the Zadoff-Chu transform (ZCT), Walsh-Hadamard transform (WHT), and discrete cosine transform (DCT) were used for PAPR reduction. However, the effect of these precoders on OTFS has not been investigated yet for PAPR reduction. In this work, we propose these precoders to reduce the high PAPR of OTFS modulation. Computer simulation results show that using these transforms as precoder in OTFS leads to significant PAPR reduction with a small error performance compromise.

In this chapter, the system model, precoding matrices, and simulation results of the proposed scheme are given.

5.1 System Model of Proposed Scheme

In this section, we introduce the proposed system model, the generation of the precoder matrices, and the PAPR expression of the OTFS signal.

5.1.1 Transmission of Proposed Scheme

We consider an OTFS system model has a bandwidth of $M\Delta f$ Hz and a total frame duration of NT seconds, where M, N are the number of subcarriers and the symbols, respectively, and $\Delta f = 1/T$ is the subcarrier spacing. Fig. 5.1 shows

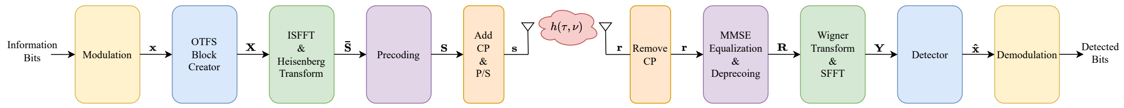

Figure 5.1: Transceiver scheme of the proposed OTFS system.

the proposed OTFS system model. Let us define $\mathbf{x} \in \mathbb{C}^{MN \times 1}$ as the modulated information symbols. Then, the elements of $\mathbf{x}$ are placed in the two-dimensional delay-Doppler grid $\mathbf{X} \in \mathbb{C}^{M \times N}$. $\mathbf{X}$ is converted to the time-frequency domain by using ISFFT, and after, using the Heisenberg transform with rectangular pulses, time-domain transmit signal matrix $\bar{\mathbf{S}} \in \mathbb{C}^{M \times N}$ can be expressed as

$$\bar{\mathbf{S}} = \mathbf{F}_M^{\mathrm{H}}(\mathbf{F}_M \mathbf{X} \mathbf{F}_N^{\mathrm{H}}) = \mathbf{X}\mathbf{F}_N^{\mathrm{H}}, \tag{5.1}$$

where $\mathbf{F}_M$ is the normalized M-point discrete Fourier transform (DFT) matrix and $(\cdot)^{\mathrm{H}}$ states Hermitian transpose operator. In the next step, the precoder is applied to the time domain signal $\bar{\mathbf{S}}$

$$\mathbf{S} = \bar{\mathbf{S}}\mathbf{P}, \tag{5.2}$$

where $\mathbf{S} \in \mathbb{C}^{M \times N}$ is the precoded time domain matrix and $\mathbf{P} \in \mathbb{C}^{N \times N}$ is the unitary precoding matrix. For transmission, $\mathbf{S}$ is column-wise vectorized by the $\mathrm{vec}(\cdot)$ operator and the transmission signal $\mathbf{s} \in \mathbb{C}^{MN \times 1}$ is obtained and transmitted over the time-varying channel

$$\mathrm{s} = \mathrm{vec}(\mathbf{S}). \tag{5.3}$$

Before transmission, a CP is added to $\mathbf{s}$ in order to prevent ISI. The time-varying channel response is represented by

$$h(\tau, \nu) = \sum_{i=1}^{P} h_i \delta(\tau - \tau_i)\delta(\nu - \nu_i), \tag{5.4}$$

where P is the number of propagation paths, h_i, τ_i and ν_i stand for the complex channel gain, delay shift and Doppler shift for the ith path, respectively.

At the receiver, after discarding CP, the received time domain signal $\mathbf{r} \in \mathbb{C}^{MN \times 1}$ can be expressed as

$$\mathbf{r} = \mathbf{H}\mathbf{s} + \mathbf{w}, \tag{5.5}$$

where $\mathbf{w} \in \mathbb{C}^{MN\times 1}$ is vector of zero mean AWGN samples with $\mathcal{CN}(0, N_0\mathbf{I}_{MN})$, N_0 is the noise variance, and $\mathbf{H} \in \mathbb{C}^{MN\times MN}$ is the time domain channel matrix [Gao and Zheng, 2020]. After receiving, the signal is equalized with minimum mean square error (MMSE) equalizer

$$\hat{\mathbf{r}} = \mathbf{H}^{\mathrm{H}}(\mathbf{H}\mathbf{H}^{\mathrm{H}} + N_0\mathbf{I}_{MN})^{-1}\mathbf{r}. \tag{5.6}$$

After exploiting the MMSE equalizer, the equalized data $\hat{\mathbf{r}}$ is de-vectorized to size $M \times N$ by $\mathrm{vec}^{-1}_{M,N}(\cdot)$ operator

$$\hat{\mathbf{R}} = \mathrm{vec}^{-1}_{M,N}(\hat{\mathbf{r}}). \tag{5.7}$$

Then, deprecoding process is applied to $\hat{\mathbf{R}}$

$$\mathbf{R} = \hat{\mathbf{R}}\mathbf{P}^{\mathrm{H}}, \tag{5.8}$$

where $\mathbf{R} \in \mathbb{C}^{M\times N}$. After that, the delay-Doppler domain received signal $\mathbf{Y}$ is obtained by applying Wigner transform and SFFT to $\mathbf{R}$ and it can be expressed as

$$\mathbf{Y} = \mathbf{F}_M^{\mathrm{H}}(\mathbf{F}_M\mathbf{R})\mathbf{F}_N = \mathbf{R}\mathbf{F}_N. \tag{5.9}$$

Finally, with the help of a detector, the delay-Doppler domain information symbol vector $\hat{\mathbf{x}}$ can be obtained by detecting symbols in $\mathrm{vec}(\mathbf{Y})$.

5.1.2 PAPR of the OTFS Signal

On the transmitter side, the PAPR of OTFS system can be expressed as [Surabhi et al., 2019b]

$$\mathrm{PAPR} = \frac{\max\,[|s(t)|^2]}{E\{|s(t)|^2\}}, \tag{5.10}$$

where $E\{\cdot\}$ corresponds to expectation operator. For a rectangular pulsed OTFS system, the maximum PAPR can be given as [Surabhi et al., 2019b]

$$\mathrm{PAPR}_{\max} = \frac{N \max_i\{|x[i]|^2\}}{E\{|x[i]|^2\}}, \tag{5.11}$$

where $i = 0, \ldots, MN-1$ and $x[i]$ is the delay-Doppler domain symbols. When (5.11) is examined, the maximum PAPR of the OTFS signal increases linearly based on the number of symbols N. Furthermore, as PAPR is a random variable, it is possible to use the complementary cumulative distribution function (CCDF) to describe the statistical features of PAPR. Given the reference level $\gamma > 0$, the possibility of the PAPR being higher than the reference value is determined by CCDF, and it can be described as

$$\mathrm{CCDF}(\gamma) = \Pr(\mathrm{PAPR} > \gamma), \tag{5.12}$$

where $\Pr(\cdot)$ represents the probability function.

5.2 Precoding Matrices

In this section, we present the generation steps of the precoding matrices. Note that all precoding matrices must be normalized to keep the signal power same.

5.2.1 Zadoff-Chu Transform Matrix

Zadoff-Chu sequences belong to a category of polyphase sequences that exhibit optimal correlation characteristics. These sequences possess perfect periodic autocorrelation and a constant amplitude. Perfect periodic autocorrelation property ensures that the energy of the precoded signal is not concentrated at specific time instances, leading to a reduction in the peak points of the signal in the time domain. A Zadoff-Chu sequence $\mathbf{z} \in \mathbb{C}^{K\times 1}$ can be defined as

$$z[k] = \begin{cases} e^{\frac{j2\pi r}{K}(\frac{k^2}{2}+qk)}, & K \text{ is even} \\ e^{\frac{j2\pi r}{K}(\frac{k(k+1)}{2}+qk)}, & K \text{ is odd} \end{cases}, \tag{5.13}$$

where $k = 0, \ldots, K-1$, r is the root index relatively prime to K and the q is any integer [Baig and Jeoti, 2010]. For the ZCT precoding matrix $\mathbf{Z}_N \in \mathbb{C}^{N\times N}$, the value of K must be chosen as N^2 when generating the ZC sequence. To obtain $\mathbf{Z}_N$, $\mathbf{z}$ is reshaped as

$$Z_N[m,l] = z[m + lN], \tag{5.14}$$

where $m = l = 0, \ldots, N-1$.

5.2.2 Walsh-Hadamard Transform Matrix

A WHT matrix has mutually orthogonal row vectors and orthogonal column vectors. The concept behind this is to utilize the orthogonal rows or columns to minimize the autocorrelation of the input sequence without the need to transmit any additional information to the receiver. Thus, WHT may reduce the occurrence of high peaks comparing the original system. A WHT matrix $\mathbf{W}_m$ is a $2^m \times 2^m$ real-valued matrix, and let us define $\mathbf{W}_0 = 1$. For $m > 0$, recursively we can express $\mathbf{W}_m$ as [Shete et al., 2016]

$$\mathbf{W}_m = \begin{bmatrix} \mathbf{W}_{m-1} & \mathbf{W}_{m-1} \\ \mathbf{W}_{m-1} & -\mathbf{W}_{m-1} \end{bmatrix}. \tag{5.15}$$

For $m > 1$, $\mathbf{W}_m$ can also defined as

$$\mathbf{W}_m = \mathbf{W}_1 \otimes \mathbf{W}_{m-1}, \tag{5.16}$$

where $\otimes$ states the Kronecker product. The $2^m = N$ condition must be satisfied to obtain the WHT precoding matrix.

5.2.3 Discrete Cosine Transform Matrix

DCT is known for its ability to decorrelate the input signal, which means it reduces the dependencies between the neighboring samples of the input signal. This decorrelation spreads the energy more evenly across the time domain samples, leading to a reduction in the peak points of the signal. DCT precoding matrix $\mathbf{C}_N \in \mathbb{R}^{N\times N}$ can be generated as [Sun et al., 2008]

$$C_N[m,l] = \begin{cases} \frac{1}{\sqrt{N}}, & m = 0, 0 \le l \le N-1 \\ \sqrt{\frac{2}{N}} \cos \frac{\pi(2l+1)m}{2N}, & \begin{array}{c} 1 \le m \le N-1, \\ 0 \le l \le N-1 \end{array} \end{cases}. \tag{5.17}$$

5.3 Simulation Results And Comparisons

In this section, the PAPR and BER performances of conventional OTFS and the proposed system are examined and compared. In all computer simulations, we

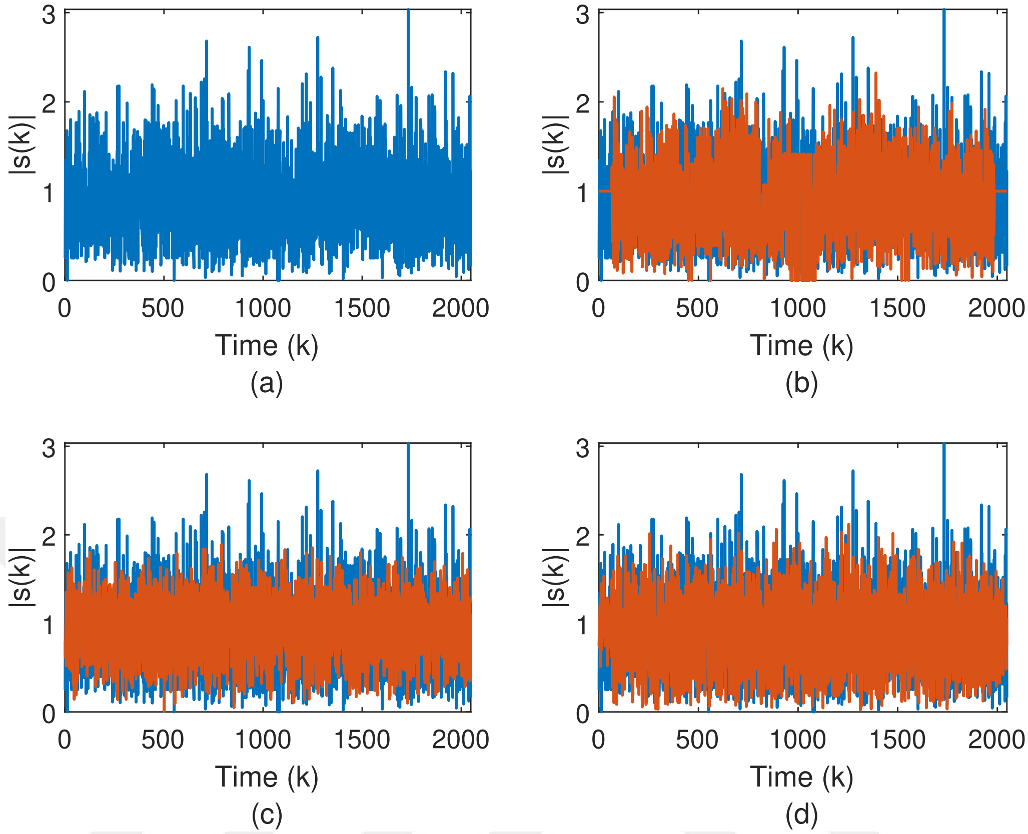

Figure 5.2: Magnitudes of (a) classical OTFS, (b) WHT precoded OTFS, (c) ZCT precoded OTFS, and (d) DCT precoded OTFS; for $N = 32, M = 64$.

consider the OTFS system with various frame sizes. The carrier frequency is 4 GHz, Δf is set to 15 kHz, and information bits are modulated with 4-QAM modulation. We use a channel with $P = 5$ paths with a uniform power delay profile, and the delay profile is $\tau_i = [0, 2.08, 4.164, 6.246, 8.328]\,\mu s$, $i = 1, \cdots, P$, where each path has a single Doppler shift generated with Jakes' model $\nu_i = \nu_{\max} \cos(\theta_i)$, where $\nu_{\max}$ corresponds to the maximum Doppler shift depending on the receiver speed and θ_i is uniformly distributed over $[-\pi, \pi]$. The receiver speed is taken as 506 km/h, which corresponds to $\nu_{\max} = 1875$ kHz. We assume that CSI is available at the receiver. We select $q = 7$ and $r = 1$ for ZCT precoding. All simulations are performed in MATLAB.

The magnitudes of classical OTFS signal and precoded schemes are given in Fig. 5.2. Since precoding matrices are unitary, the average power is same. However, as

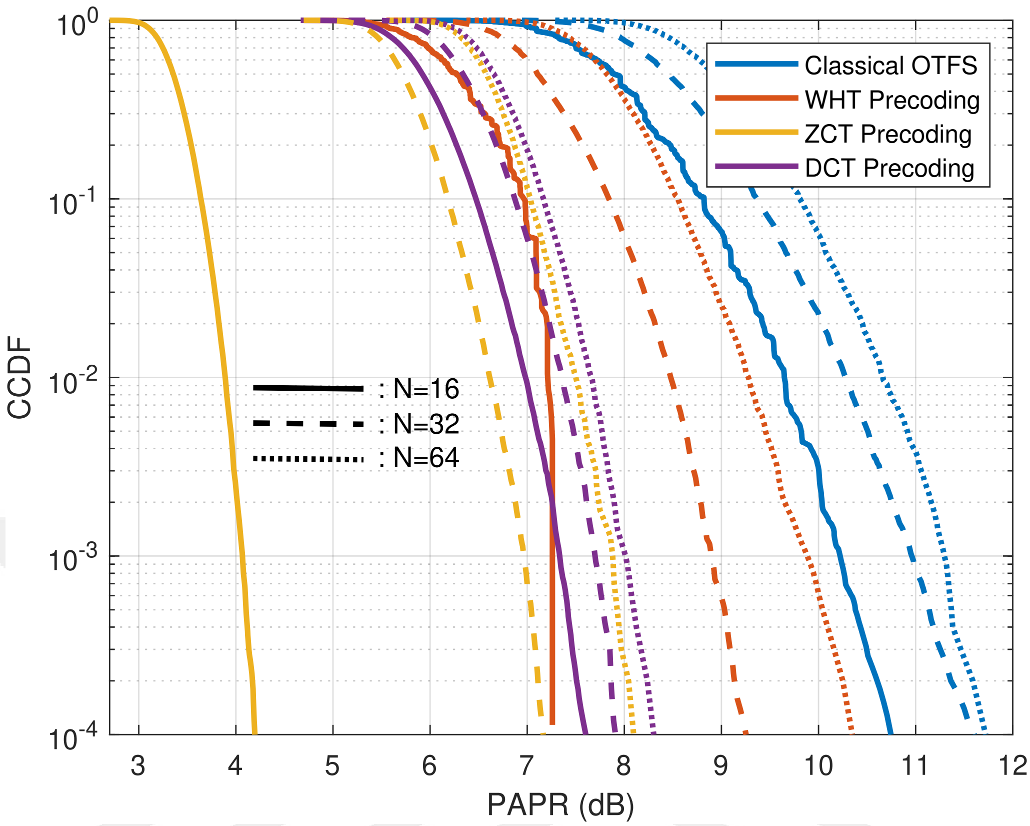

Figure 5.3: CCDF of the PAPR for $M = 64$ and $N = 16, 32, 64$.

we can see from the figure, precoded schemes have smaller peak points. Therefore, precoded schemes exhibit reduced PAPR levels.

In Fig. 5.3, the CCDF of the PAPR is examined for varying N for the classical OTFS and WHT, ZCT, and DCT precoded OTFS. The frame size is chosen as $M = 64$ and $N = 16, 32, 64$. For CCDF $= 10^{-4}$ level, in the case of $N = 16$, WHT, ZCT, and DCT precoders provide approximately 3.5 dB, 6.55 dB, and 3.15 dB PAPR gains, respectively. When $N = 32$, WHT, ZCT, and DCT precoders provide approximately 2.35 dB, 4.45 dB, and 3.7 dB PAPR gains, respectively. Finally, for $N = 64$, WHT, ZCT, and DCT precoders provide approximately 1.4 dB, 3.6 dB, and 3.4 dB PAPR gains, respectively. From the figure, while all precoded OTFS systems show better PAPR performance than classical OTFS, the ZCT precoding has the best PAPR performance among precoders for all N. Furthermore, PAPR performance decreases for all systems when N is increased.

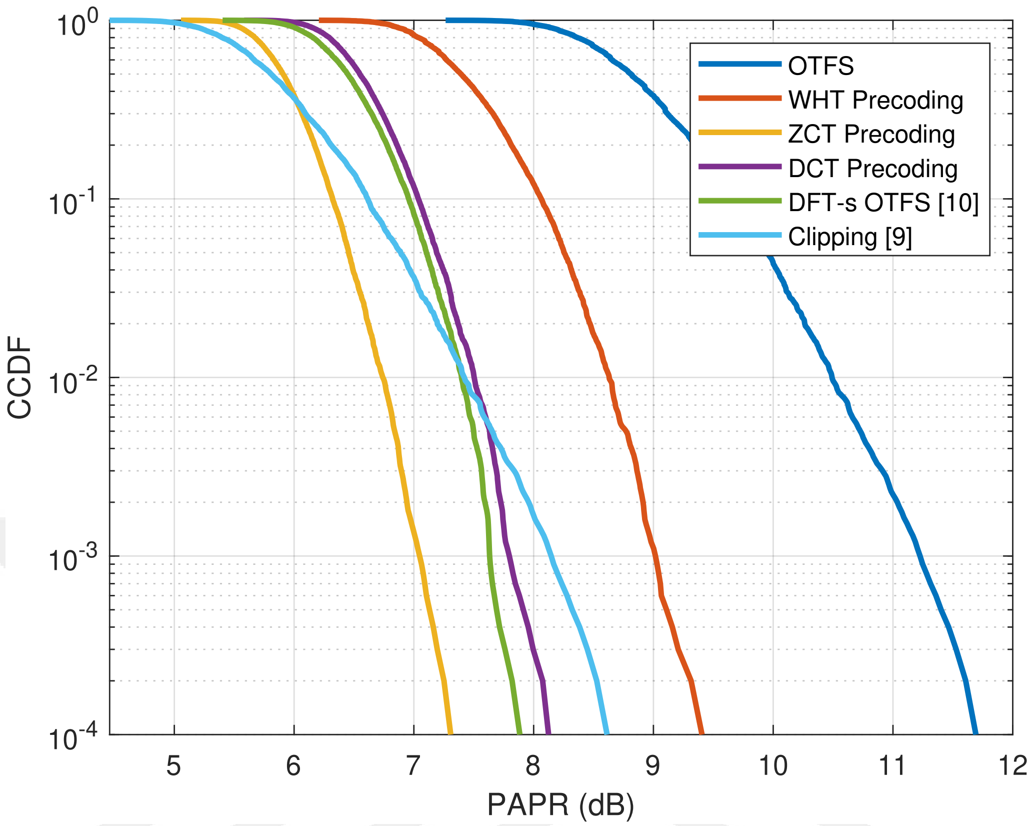

Figure 5.4: PAPR performance comparison for proposed and different PAPR reduction schemes while $N = 32, M = 64$.

Fig. 5.4 shows the PAPR performances of the classical OTFS, proposed method, clipping in [Tek et al., 2020] and DFT-s OTFS in [Wu et al., 2021]. For the DFT-s OTFS and clipping method, we choose the parameters used in the related studies as $L = 16$ and $\beta = 0.7$, respectively. When Fig. 5.4 is examined for CCDF $= 10^{-4}$, WHT precoding has a 2.3 dB gain, ZCT precoding has a 4.4 dB gain, and DCT precoding has a 3.57 dB gain. DFT-s OTFS and clipping method have 3.8 dB and 3 dB gain, respectively.

Finally, Fig. 5.5 compares the BER performance of the classical OTFS, proposed precoders, clipping technique, and DFT-s OTFS technique. For the DFT-s OTFS system, 16-QAM modulation is used to achieve the same SE as other systems. From the results, we can see that the precoding schemes cause small performance degradation and show similar BER performances. For the BER level of 10^{-5}, there

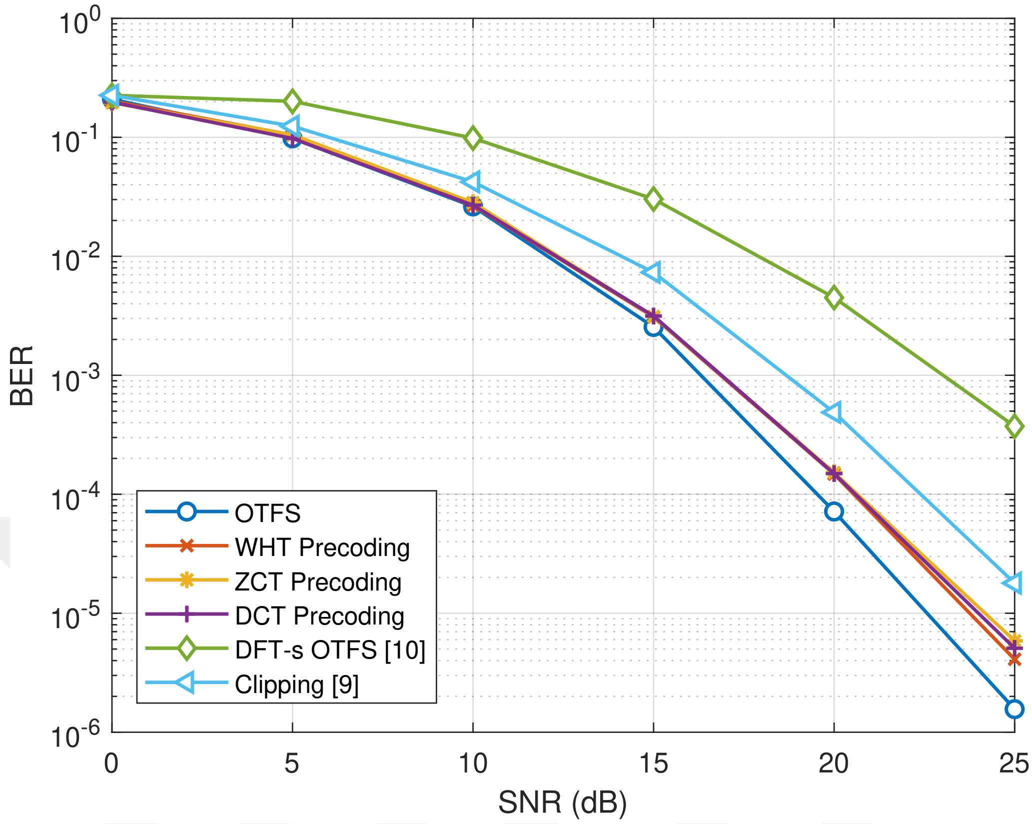

Figure 5.5: BER performance comparison for proposed and different PAPR reduction schemes while $N = 32, M = 64$.

are 1.2, 1.4, and 1.6 dB differences between classical OTFS and WHT, ZCT, and DCT precoders, respectively. The reason for this degradation can be explained by the fact that a little ISI remains after the MMSE equalizer. The performance of delay-Doppler domain symbols depends on the average of all symbols in the time-frequency domain [Tie et al., 2022]. Since we apply deprecoding in the time domain, and due to residual ISI, the BER performance is affected. Even though clipping and DFT-s OTFS methods have similar PAPR performances with precoding schemes, their BER performances are worse than the classical OTFS and the precoded OTFS schemes.

Chapter 6

CONCLUSIONS

In this thesis, by utilizing DL, index modulation IM, and the unitary matrices, three different solutions are presented in order to improve the performance metrics of OTFS modulation.

First, an AE-based scheme to improve the error performance of OTFS by learning a set of n-dim symbols and maximizing the SMED between them is proposed. Using an AWGN channel instead of a doubly-dispersive channel provides a simple AE structure to be trained. The encoder and decoder of AE are used as the mapper and demapper blocks of a real-time OTFS system after training them under the AWGN channel. Moreover, a theoretical FER upper bound has been derived. Computer simulation results show that, in terms of the FER performance, AEE-OTFS performs better than the conventional OTFS system. In addition, LD significantly reduces the decoding complexity. We conclude that the proposed AEE-OTFS scheme can be a candidate for certain 6G use cases thanks to its outstanding error performance in the presence of high mobility and flexibility.

Secondly, a block-wise IM scheme called JDDIM-OTFS aimed at enhancing the error performance of OTFS is introduced. Furthermore, a theoretical upper bound on the BER is derived. Computer simulations demonstrated that JDDIM-OTFS outperforms conventional OTFS, OTFS-IM, and DeIM-OTFS systems in terms of BER performance when coupled with MFGS-ML and MFGS-GRD detectors. Additionally, using a Greedy detector in MFGS significantly reduces decoding complexity. The proposed JDDIM-OTFS scheme exhibits exceptional error performance in scenarios with high mobility and flexibility, which can make it a viable option for specific 6G use cases.

Lastly, using WHT, ZCT, and DCT unitary transformations to reduce the high PAPR values of OTFS is proposed, and their performances are investigated. The

PAPR performance of the proposed method has been investigated for different frame sizes and compared with clipping and DFT-s OTFS methods. In addition, the BER performance of the proposed method has also been examined and compared with other mentioned methods. Computer simulation results show that the proposed method provides significant PAPR gains while compromising the error performance by about 1.5 dB. Remarkable PAPR gains and no need for side information on the receiver make the proposed method significant.

Considering the needs of next-generation communication systems, OTFS is seen as the most important waveform candidate. Its superior performance in the double-dispersive channel makes it suitable for 6G scenarios. However, rapidly developing technology and reliable data transfer needed in high-speed scenarios require superior waveforms in terms of performance metrics. In this thesis study, three novel methods that improve the error performance and PAPR performance of OTFS have been presented to meet this need. Simulation studies show that the proposed methods can easily find a place in next-generation communication systems.

BIBLIOGRAPHY

[Baig and Jeoti, 2010] Baig, I. and Jeoti, V. (2010). PAPR reduction in OFDM systems: Zadoff-Chu matrix transform based pre/post-coding techniques. In *2nd Int. Conf. Computational Intell., Commun. Syst. and Netw.*

[Basar et al., 2013] Basar, E., Aygolu, U., Panayirci, E., and Poor, H. V. (2013). Orthogonal frequency division multiplexing with index modulation. *IEEE Transactions on Signal Processing*, 61(22):5536–5549.

[Bitra et al., 2022a] Bitra, H., Ponnusamy, P., and Chintagunta, S. (2022a). Reduction of PAPR in OTFS using normalized μ-law and A-law companding transform. *Internet Technology Letters*, 5(3):e344.

[Bitra et al., 2022b] Bitra, H., Ponnusamy, P., Chintagunta, S., and Pragadeshwaran, S. (2022b). Nonlinear companding transforms for reducing the PAPR of OTFS signal. *Physical Communications*, 53:101729.

[ETSI TS 136 104 V14.3.0, 2017] ETSI TS 136 104 V14.3.0 (2017). Evolved Universal Terrestrial Radio Access (E-UTRA); Base Station (BS) radio transmission and reception.

[Feng et al., 2022] Feng, D., Zheng, J., Bai, B., Jiang, J., and Zheng, L. (2022). In-phase and quadrature index modulation aided OTFS transmission. *IEEE Communications Letters*, 26(6):1318–1322.

[Francis et al., 2021] Francis, J. K., Mary Augustine, R., and Chockalingam, A. (2021). Diversity and PAPR enhancement in OTFS using indexing. In *2021 IEEE 93rd Vehicular Technology Conference (VTC2021-Spring)*, pages 1–6.

[Gao and Zheng, 2020] Gao, S. and Zheng, J. (2020). Peak-to-average power ratio reduction in pilot-embedded OTFS modulation through iterative clipping and filtering. *IEEE Commun. Lett.*, 24(9):2055–2059.

[Hadani et al., 2017] Hadani, R., Rakib, S., Tsatsanis, M., Monk, A., Goldsmith, A. J., Molisch, A. F., and Calderbank, R. (2017). Orthogonal time frequency space modulation. In *2017 IEEE Wireless Communications and Networking Conference (WCNC)*, pages 1–6.

[Han and Lee, 2005] Han, S. H. and Lee, J. H. (2005). An overview of peak-to-average power ratio reduction techniques for multicarrier transmission. *IEEE Wireless Commun.*, 12(2):56–65.

[Hossain et al., 2020] Hossain, M. N., Sugiura, Y., Shimamura, T., and Ryu, H.-G. (2020). DFT-spread OTFS communication system with the reductions of PAPR and nonlinear degradation. *Wireless Personal Communications*, 115(3):2211–2228.

[Li et al., 2021] Li, S., Yuan, J., Yuan, W., Wei, Z., Bai, B., and Ng, D. W. K. (2021). Performance analysis of coded OTFS systems over high-mobility channels. *IEEE Transactions on Wireless Communications*, 20(9):6033–6048.

[Liang et al., 2020] Liang, Y., Li, L., Fan, P., and Guan, Y. (2020). Doppler resilient orthogonal time-frequency space (OTFS) systems based on index modulation. In *2020 IEEE 91st Vehicular Technology Conference (VTC2020-Spring)*, pages 1–5.

[Liu et al., 2023] Liu, C., Li, S., Yuan, W., Liu, X., and Ng, D. W. K. (2023). Predictive precoder design for OTFS-enabled URLLC: A deep learning approach. *IEEE Journal on Selected Areas in Communications*, 41(7):2245–2260.

[Liu et al., 2021] Liu, M., Zhao, M.-M., Lei, M., and Zhao, M.-J. (2021). Autoencoder based PAPR reduction for OTFS modulation. In *Proc. IEEE 94th Veh. Technol. Conf. (VTC2021-Fall)*.

[Mohammed, 2021] Mohammed, S. K. (2021). Derivation of OTFS modulation from first principles. *IEEE Transactions on Vehicular Technology*, 70(8):7619–7636.

[Naikoti and Chockalingam, 2021] Naikoti, A. and Chockalingam, A. (2021). Low-complexity delay-doppler symbol dnn for OTFS signal detection. In *2021 IEEE 93rd Vehicular Technology Conference (VTC2021-Spring)*, pages 1–6.

[Naveen and Sudha, 2020] Naveen, C. and Sudha, V. (2020). Peak-to-average power ratio reduction in OTFS modulation using companding technique. In *5th Int. Conf. Devices, Circuits and Syst. (ICDCS)*, pages 140–143.

[Park et al., 2023] Park, J., Hong, J.-P., Kim, H., and Jeong, B. J. (2023). Auto-encoder based orthogonal time frequency space modulation and detection with meta-learning. *IEEE Access*, 11:43008–43018.

[Qian et al., 2023] Qian, M., Ji, F., Ge, Y., Wen, M., Cheng, X., and Vincent Poor, H. (2023). Block-wise index modulation and receiver design for high-mobility OTFS communications. *IEEE Transactions on Communications*, pages 1–1.

[Raviteja et al., 2020] Raviteja, P., Hong, Y., Viterbo, E., and Biglieri, E. (2020). Effective diversity of OTFS modulation. *IEEE Wireless Communications Letters*, 9(2):249–253.

[Raviteja et al., 2018] Raviteja, P., Phan, K. T., Hong, Y., and Viterbo, E. (2018). Interference cancellation and iterative detection for orthogonal time frequency space modulation. *IEEE Trans. Wireless Commun.*, 17(10):6501–6515.

[Raviteja et al., 2019] Raviteja, P., Viterbo, E., and Hong, Y. (2019). OTFS performance on static multipath channels. *IEEE Wireless Communications Letters*, 8(3):745–748.

[Ren et al., 2021] Ren, H., Xu, W., and Wang, L. (2021). Orthogonal time-frequency space with improved index modulation. In *2021 15th International*

Conference on Signal Processing and Communication Systems (ICSPCS), pages 1–6.

[Ren et al., 2022] Ren, H., Xu, W., and Wang, L. (2022). Multiple-mode orthogonal time frequency space with index modulation. *Electronics*, 11(16):2600.

[Shete et al., 2016] Shete, S., Bhide, G., and Jadhav, M. (2016). WHT and double WHT: An effective PAPR reduction approach in OFDM. In *IEEE Int. Conf. on Adv. in Electron., Commun. and Computer Tech. (ICAECCT)*.

[Su et al., 2022] Su, J., Liu, S., Huang, Y., and Yuan, J. (2022). Peak-to-average power ratio reduction via symbol precoding in OTFS modulation. In *Proc. IEEE 95th Veh. Technol. Conf. (VTC2022-Spring)*.

[Sui et al., 2023] Sui, Z., Yan, S., Zhang, H., Sun, S., Zeng, Y., Yang, L.-L., and Hanzo, L. (2023). Performance analysis and approximate message passing detection of orthogonal time sequency multiplexing modulation. *IEEE Trans. Wireless Commun.* early access.

[Sun et al., 2008] Sun, S., Hou, C., Yan, L., and Fu, J. (2008). A novel method based DCT to reduce PAPR of OFDM systems. In *4th Int. Conf. Wireless Commun., Netw. and Mobile Comput.*

[Surabhi et al., 2019a] Surabhi, G. D., Augustine, R. M., and Chockalingam, A. (2019a). On the diversity of uncoded OTFS modulation in doubly-dispersive channels. *IEEE Transactions on Wireless Communications*, 18(6):3049–3063.

[Surabhi et al., 2019b] Surabhi, G. D., Augustine, R. M., and Chockalingam, A. (2019b). Peak-to-average power ratio of OTFS modulation. *IEEE Commun. Lett.*, 23(6):999–1002.

[Sümer et al., 2022] Sümer, A. S., Yılmaz, T., Memişoğlu, E., and Arslan, H. (2022). Exploiting OTFS frame structure for PAPR reduction. In *Proc. IEEE 96th Veh. Technol. Conf. (VTC2022-Fall)*.

[Tek et al., 2023] Tek, Y. I., Dogukan, A. T., and Basar, E. (2023). Autoencoder-based enhanced orthogonal time frequency space modulation. *IEEE Commun. Lett.* early access.

[Tek et al., 2020] Tek, Y. I., Yasar, S., Sinop, H., Karaerik, K., Tuna, E. B., and Ozen, A. (2020). PAPR reduction method for next generation waveforms. In *28th Signal Process. and Commun. Appl. Conf. (SIU)*.

[Thaj and Viterbo, 2020] Thaj, T. and Viterbo, E. (2020). Low complexity iterative rake decision feedback equalizer for zero-padded OTFS systems. *IEEE Trans. Veh. Technol.*, 69(12):15606–15622.

[Thaj et al., 2021] Thaj, T., Viterbo, E., and Hong, Y. (2021). Orthogonal time sequency multiplexing modulation: Analysis and low-complexity receiver design. *IEEE Trans. Wireless Commun.*, 20(12):7842–7855.

[Tie et al., 2022] Tie, Z., Shi, J., Yan, S., Wu, K., and Li, Z. (2022). Optimal power allocation for OTFS with frequency-domain linear equalizers. *IEEE Commun. Lett.*, 26(11):2715–2719.

[Wei et al., 2022] Wei, P., Xiao, Y., Feng, W., Ge, N., and Xiao, M. (2022). Charactering the peak-to-average power ratio of OTFS signals: A large system analysis. *IEEE Trans. Wireless Commun.*, 21(6):3705–3720.

[Wu et al., 2021] Wu, Y., Han, C., and Yang, T. (2021). DFT-spread orthogonal time frequency space modulation design for terahertz communications. In *IEEE Global Commun. Conf. (GLOBECOM)*.

[Xu et al., 2020] Xu, X., Zhao, M.-M., Lei, M., and Zhao, M.-J. (2020). A damped gamp detection algorithm for OTFS system based on deep learning. In *2020 IEEE 92nd Vehicular Technology Conference (VTC2020-Fall)*, pages 1–5.

[Zhang et al., 2007] Zhang, J., Jayalath, A. D. S., and Chen, Y. (2007). Asymmetric

OFDM systems based on layered FFT structure. *IEEE Signal Processing Letters*, 14(11):812–815.

[Zhao et al., 2021] Zhao, H., He, D., Kang, Z., and Wang, H. (2021). Orthogonal time frequency space (OTFS) with dual-mode index modulation. *IEEE Wireless Communications Letters*, 10(5):991–995.

[Zhou et al., 2022] Zhou, Z., Liu, L., Xu, J., and Calderbank, R. (2022). Learning to equalize OTFS. *IEEE Transactions on Wireless Communications*, 21(9):7723–7736.